

## Supplementary Information

# Charge transport through single-molecule bilayer-graphene junctions with atomic thickness

Shiqiang Zhao,<sup>a</sup> Ze-Ying Deng,<sup>a</sup> Shadiah Albalawi,<sup>b</sup> Qingqing Wu,<sup>b</sup> Lijue Chen,<sup>a</sup> Hwei Zhang,<sup>a</sup> Xin-Jing Zhao,<sup>a</sup> Hao Hou,<sup>a</sup> Songjun Hou,<sup>b</sup> Gang Dong,<sup>a</sup> Yang Yang,<sup>a</sup> Jia Shi,<sup>a</sup> Colin J. Lambert,<sup>\*b</sup> Yuan-Zhi Tan,<sup>\*a</sup> Wenjing Hong,<sup>\*a</sup>

<sup>a</sup>State Key Laboratory of Physical Chemistry of Solid Surfaces, College of Chemistry and Chemical Engineering, Xiamen University, Xiamen, 361005, China.

<sup>b</sup> Department of Physics, Lancaster University, Lancaster LA1 4YB, United Kingdom.

\*Email: [whong@xmu.edu.cn](mailto:whong@xmu.edu.cn); [yuanzhi\\_tan@xmu.edu.cn](mailto:yuanzhi_tan@xmu.edu.cn); [c.lambert@lancaster.ac.uk](mailto:c.lambert@lancaster.ac.uk)

## CONTENT

<b>Section S1 Molecular Synthesis</b> .....	2
1.1 MBLGs.....	2
1.2 MSLG-C96.....	2
<b>Section S2 Charge transport through single-molecule junctions</b> .....	12
2.1 The cross-plane break junction (XPBJ) setup .....	12
2.2 Conductance measurement.....	14
2.2.1 Pure solvent measurement.....	14
2.2.2 Single-molecule conductance measurement experiments .....	15
<b>Section S3 Theoretical calculation</b> .....	26
<b>References</b> .....	33

## Section S1 Molecular Synthesis

### 1.1 MBLGs

#### Synthesis of compounds MBLG-C96, MBLG-C108, and MBLG-C114.

MBLG-C96, MBLG-C108, and MBLG-C114 were synthesized according to previously reported literature.<sup>1, 2</sup>

### 1.2 MSLG-C96

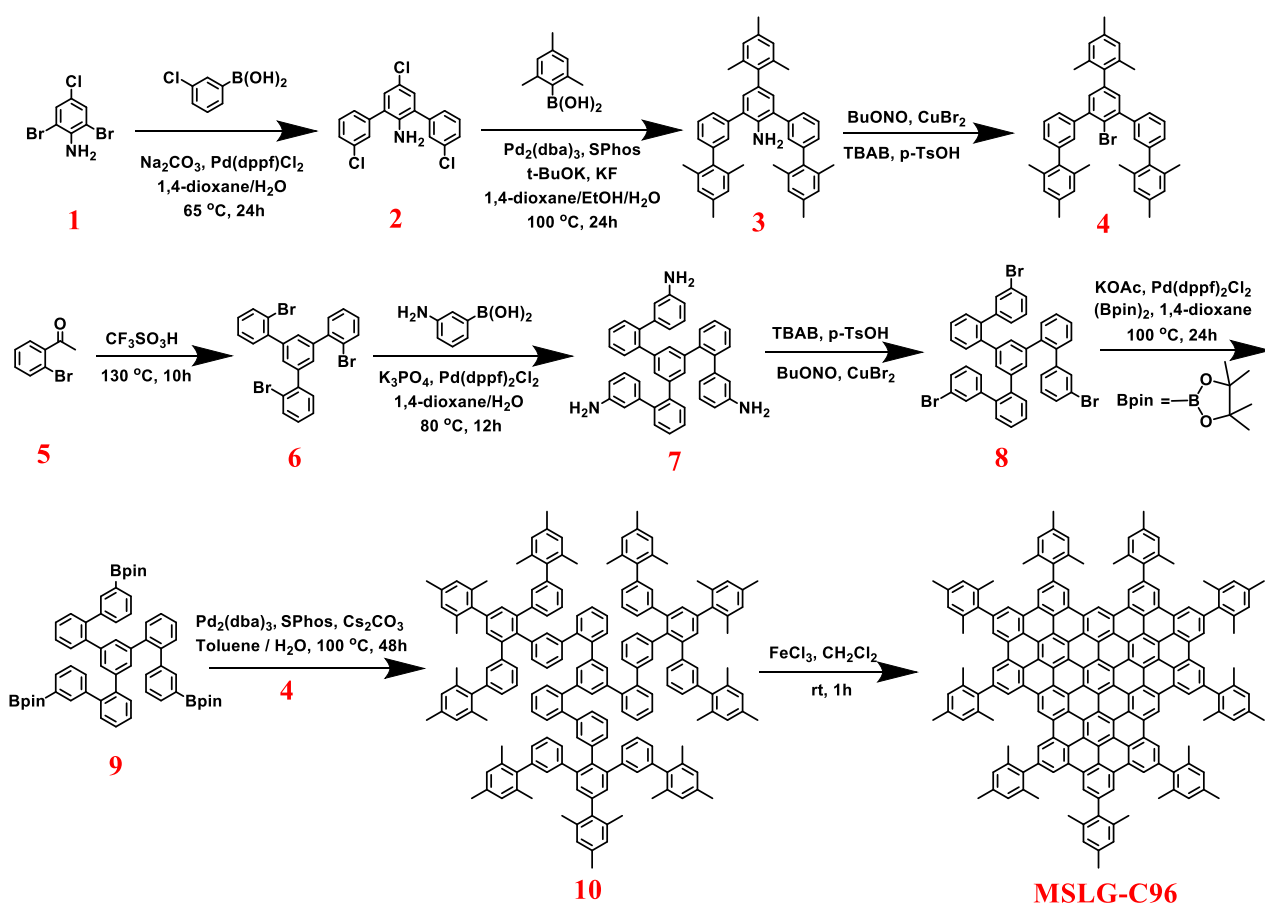
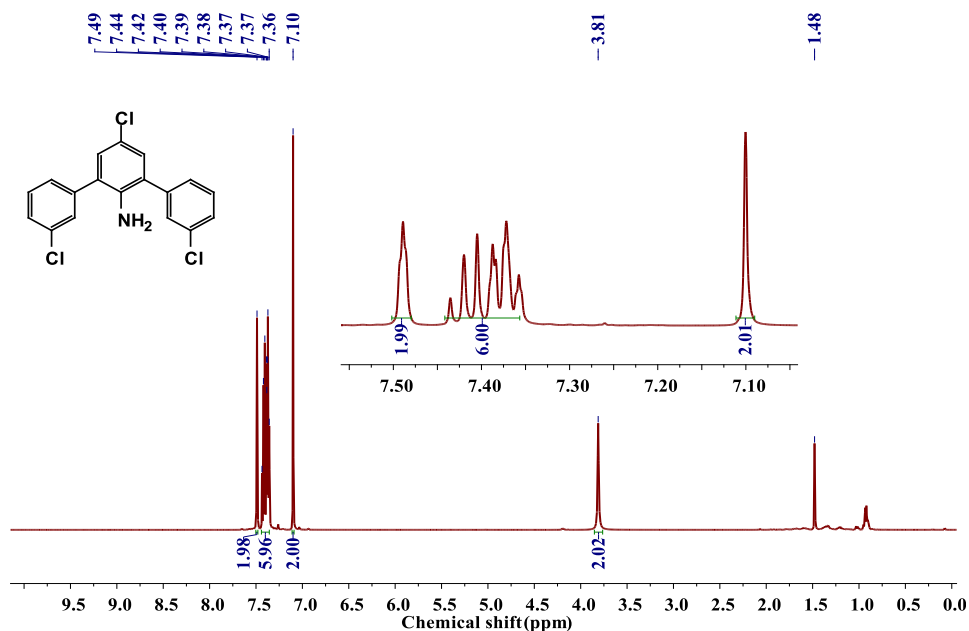


Figure S1. Synthetic route of MSLG-C96

**Synthesis of compound 2.** Compound 1 is commercially available. A mixture of **1** (2.85 g, 10.0 mmol), 3-chlorophenylboronic acid (4.69 g, 30.0 mmol), sodium carbonate (3.18 g, 30.0 mmol),  $\text{Pd(dppf)Cl}_2$  (365.9 mg, 0.50 mmol) in 1,4-dioxane (32 mL) and water (8 mL) were stirred under argon at 65 °C for 24 h. After cooling to room temperature, quenched with 1 M aqueous HCl and extracted with DCM (30 mL×3). The organic layer was collected, dried with anhydrous  $\text{MgSO}_4$  and

concentrated under reduced pressure. The crude products were then purified by silica gel column chromatography (petroleum ether/DCM=10/1 as eluent) to obtain compound **2** (3.00 g, 85.7%) as a white solid.



**Figure S2.**  $^1\text{H}$  NMR spectrum of compound **2**. (500 MHz,  $\text{CDCl}_3$ )  $\delta$  7.41 (s, 2H), 7.32 (m, 6H), 7.02 (s, 2H), 3.74 (s, 2H) ppm.

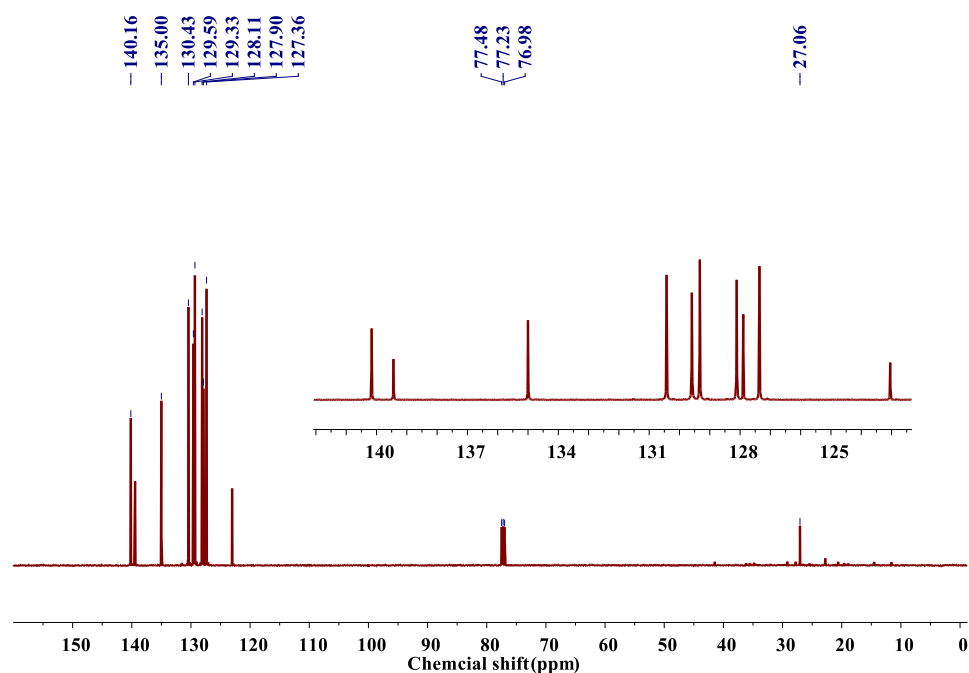


**Figure S3.**  $^{13}\text{C}$  NMR spectrum of compound **2**. (126 MHz,  $\text{CDCl}_3$ )  $\delta$  140.16, 139.44, 135.00, 130.43, 129.59, 129.33, 128.11, 127.90, 127.36, 123.05, 27.06 ppm.

**Synthesis of compound 4.** A mixture of **2** (1.75 g, 5.00 mmol), 2,4,6-trimethylphenylboronic acid (4.92 g, 30.0mmol), Pd<sub>2</sub>(dba)<sub>3</sub> (457.9 mg, 0.50 mmol), SPhos (410.0 mg, 1.00 mmol), potassium tert-butanolate (5.04 g, 45 mmol),potassium fluoride (2.61 g, 45 mmol) in 1,4-dioxane (25 mL), EtOH (8.5 mL) and H<sub>2</sub>O (7.0 mL) were stirred under argon at 80 °C for 24 h. After cooling to room temperature, the mixture was washed with water and extracted with DCM (30 mL×3). The organic layer was collected, dried with anhydrous MgSO<sub>4</sub> and concentrated under reduced pressure. The crude products were used as starting material for the next step of reaction without further purification.

To the residue, p-toluenesulfonic acid (929.8 mg, 5.40 mmol), tetrabutylammonium bromide (2.90 g, 9.00 mmol), cupric bromide (10.1 mg, 0.045 mmol), butyl nitrite (1.00 mL, 5.40 mmol) and acetonitrile (50.0 mL) were added and the mixture was stirred at room temperature for 1 h. After the mixture was quenched with H<sub>2</sub>O, the resulting solution was extracted with DCM (30 mL×3). The organic layer was collected, dried with anhydrous MgSO<sub>4</sub> and concentrated under reduced pressure. The crude products were then purified by silica gel column chromatography (petroleum ether as eluent) to obtain compound **4** (2.00 g, 60.3%) as a white solid.

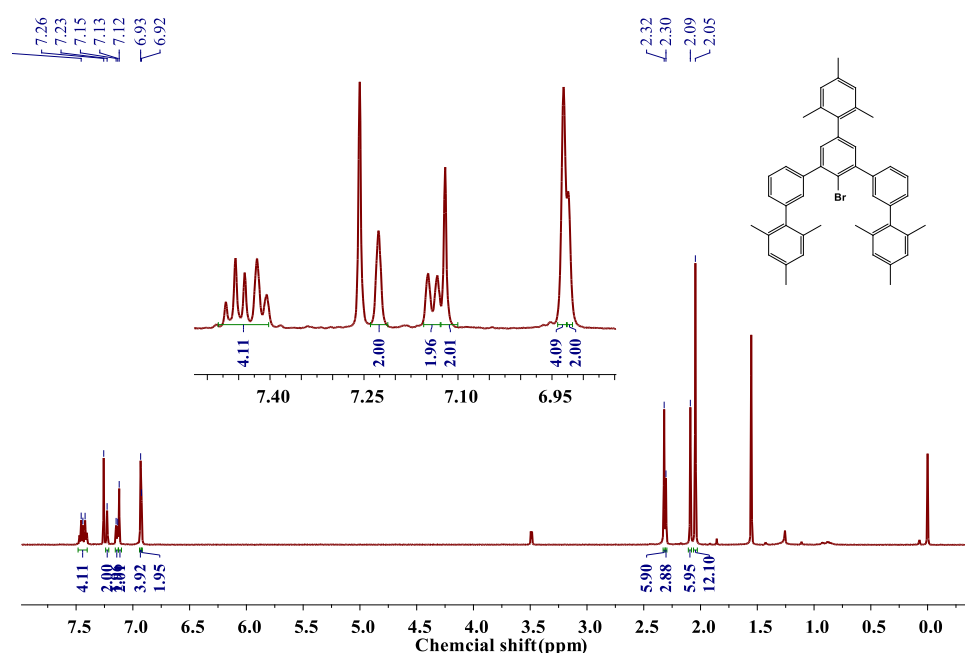


**Figure S4.** <sup>1</sup>H NMR spectrum of compound **4**. (500 MHz, CDCl<sub>3</sub>) δ 7.48 – 7.40 (m, 4H), 7.23 (s, 2H), 7.14 (d, *J* = 7.3 Hz, 2H), 7.12 (s, 2H), 6.93 (s, 4H), 6.92 (s, 2H), 2.32 (s, 6H), 2.30 (s, 3H), 2.09 (s, 6H), 2.05 (s, 12H) ppm.

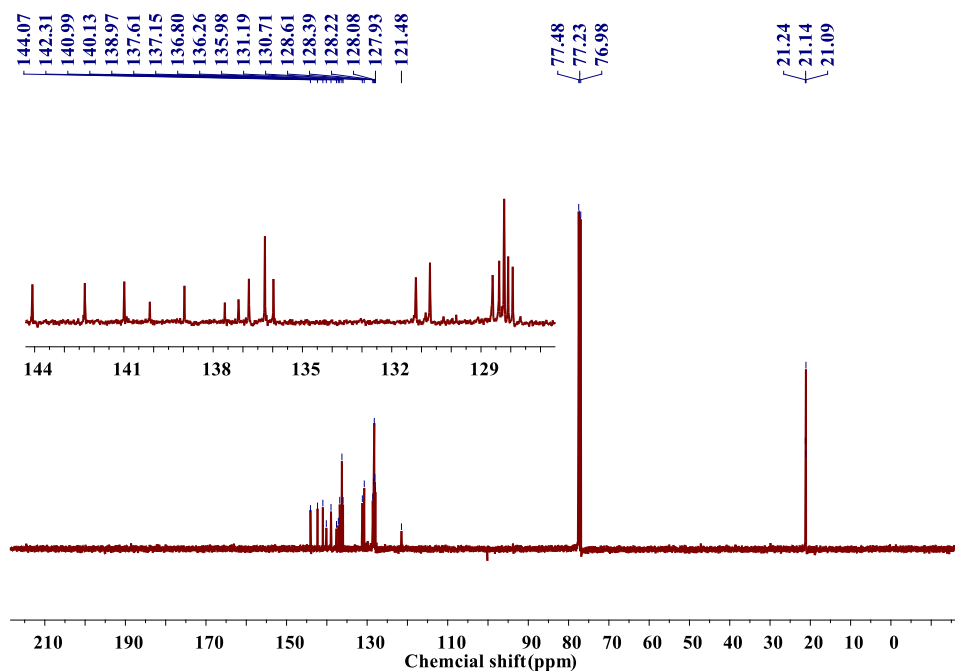


**Figure S5.**  $^{13}\text{C}$  NMR spectrum of compound **4**. (126 MHz,  $\text{CDCl}_3$ )  $\delta$  144.07, 142.31, 140.99, 140.13, 138.97, 137.61, 137.15, 136.80, 136.26, 135.98, 131.19, 130.71, 128.61, 128.39, 128.22, 128.08, 127.93, 121.48, 21.24, 21.14, 21.09 ppm.

**Synthesis of compound 6.** Compound **6** was synthesized according to previously reported literature.<sup>3</sup>

**Synthesis of compound 8.** A mixture of **6** (1.08 g, 2.00 mmol), 3-aminobenzenboronic acid (1.23 g, 9.00 mmol),  $\text{K}_3\text{PO}_4$  (3.82 g, 18 mmol),  $\text{Pd}(\text{dppf})\text{Cl}_2$  (146.3 mg, 0.20 mmol) in 1,4-dioxane (16 mL) and water (4 mL) were stirred under argon at 80 °C for 12 h. After cooling to room temperature, the mixture was washed with water and extracted with DCM (30 mL $\times$ 3). The organic layer was collected, dried with anhydrous  $\text{MgSO}_4$  and concentrated under reduced pressure. The crude products were used as starting material for the next step of reaction without further purification.

To the residue, p-toluenesulfonic acid (1.15 g, 6.48 mmol), tetrabutylammonium bromide (3.48 g, 10.8 mmol), cupric bromide (12.06 mg, 0.054 mmol), butyl nitrite (0.90 mL, 6.48 mmol) and acetonitrile (20.0 mL) were added and the mixture was stirred at 40 °C for 6 h. After the mixture was quenched with  $\text{H}_2\text{O}$ , the resulting solution was extracted with DCM (30 mL $\times$ 3). The organic layer was collected, dried with anhydrous  $\text{MgSO}_4$  and concentrated under reduced pressure. The crude products were then purified by silica gel column chromatography (petroleum ether as eluent) to obtain

compound **8** (0.942 g, 61.4%) as a white solid.

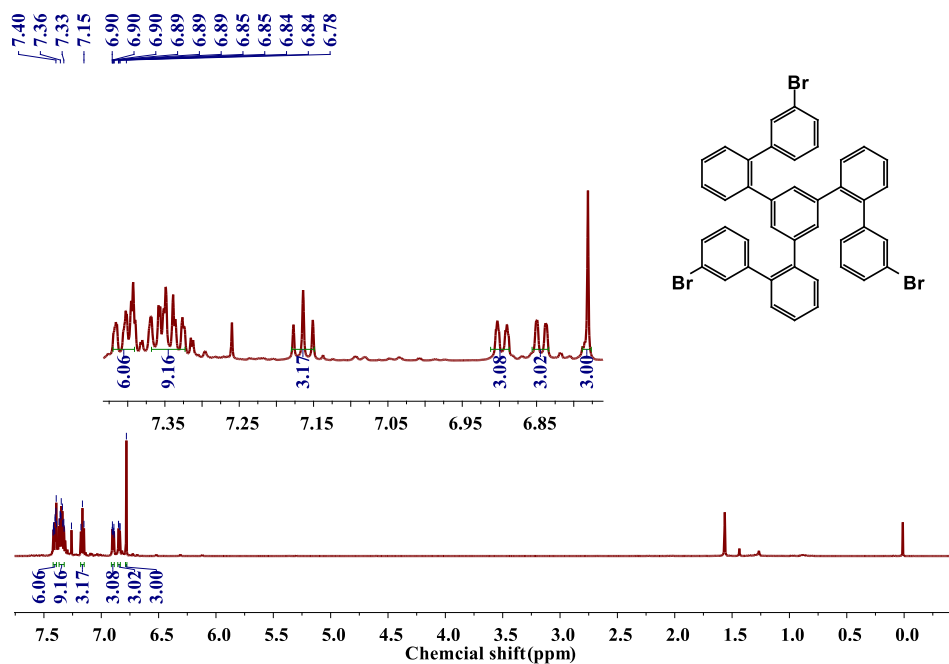


**Figure S6.**  $^1\text{H}$  NMR spectrum of compound **8**. (500 MHz,  $\text{CDCl}_3$ )  $\delta$  7.43 – 7.31 (m, 15H), 7.16 (t,  $J = 7.8$  Hz, 3H), 6.92 – 6.88 (m, 3H), 6.84 (m, 3H), 6.78 (s, 3H) ppm.

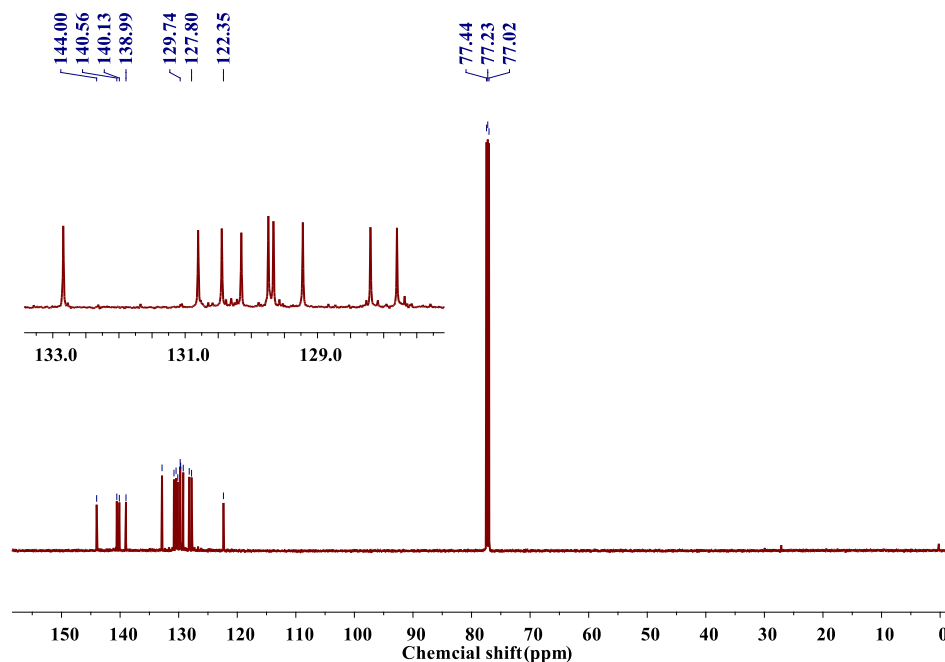


**Figure S7.**  $^{13}\text{C}$  NMR spectrum of compound **8**. (126 MHz,  $\text{CDCl}_3$ )  $\delta$  144.00, 140.56, 140.13, 138.99, 132.84, 130.80, 130.44, 130.15, 129.74, 129.67, 129.22, 128.20, 127.80, 122.35 ppm.

**Synthesis of compound 9.** A mixture of **8** (0.500 g, 0.652 mmol), bis(pinacolato)diboron (1.49 g, 5.89 mmol), potassium acetate (0.576 g, 5.89 mmol), Pd(dppf)Cl<sub>2</sub> (146.3 mg, 0.20 mmol) in 1,4-dioxane (10 mL) were stirred under argon at 100 °C for 24 h. After cooling to room temperature, the mixture was washed with water and extracted with EtOAc (10 mL×3). The organic layer was collected, dried with anhydrous MgSO<sub>4</sub> and concentrated under reduced pressure. The crude products were then purified by silica gel column chromatography (petroleum ether/ EtOAc =10:1 as eluent) to obtain compound **9** (0.300 g, 50.6%) as a white solid.

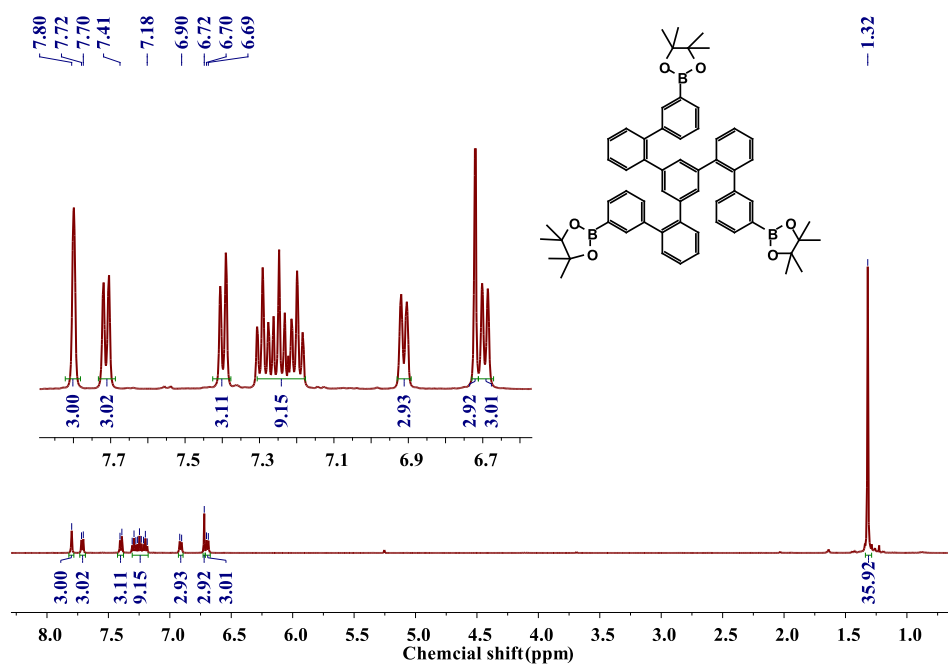


**Figure S8.** <sup>1</sup>H NMR spectrum of compound **9**. (500 MHz, CDCl<sub>3</sub>) δ 7.80 (s, 3H), 7.71 (d, *J* = 7.3 Hz, 3H), 7.40 (d, *J* = 7.6 Hz, 3H), 7.24 (m, 3H), 6.91 (d, *J* = 7.7 Hz, 3H), 6.72 (s, 1H), 6.69 (d, *J* = 7.6 Hz, 1H), 1.32 (s, 36H) ppm.

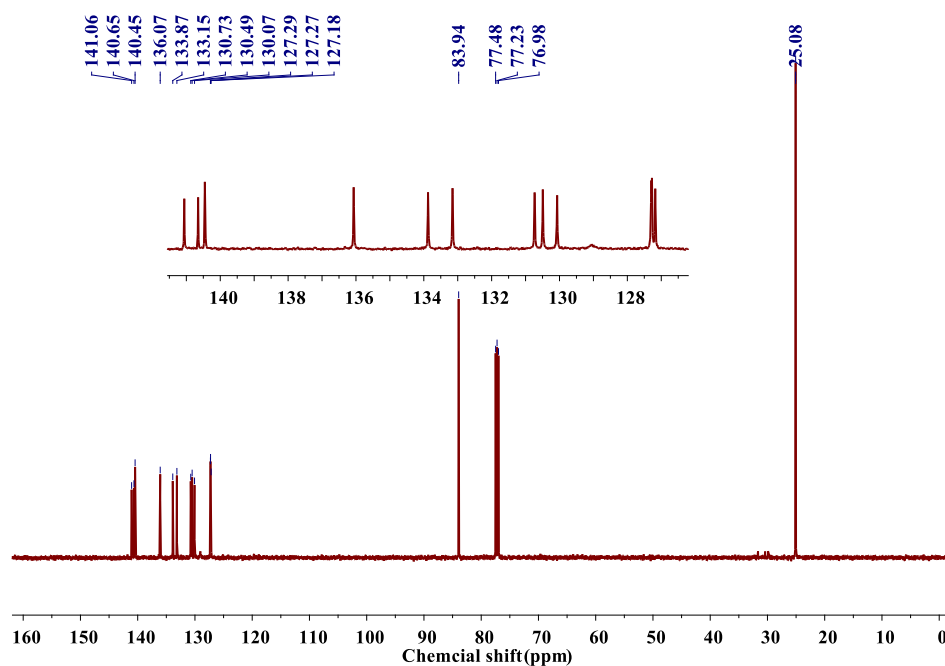


**Figure S9.**  $^{13}\text{C}$  NMR spectrum of compound **9**. (126 MHz,  $\text{CDCl}_3$ )  $\delta$  141.06, 140.65, 140.45, 136.07, 133.87, 133.15, 130.73, 130.49, 130.07, 127.29, 127.27, 127.18, 83.94, 25.08 ppm.

**Synthesis of compound 10.** A mixture of **9** (50.0 mg, 0.0549 mmol), compound **4** (327.5 mg, 0.494mmol),  $\text{Pd}_2(\text{dba})_3$  (30.2 mg, 0.0329 mmol), SPhos (27.0 mg, 0.0659 mmol), cesium carbonate (160.9 mg, 0.494 mmol) in toluene (2 mL) and water (1 mL) were stirred under argon at 100 °C for 48 h. After cooling to room temperature, the mixture was washed with water and extracted with DCM (10 mL $\times$ 3). The organic layer was collected, dried with anhydrous  $\text{MgSO}_4$  and concentrated under reduced pressure. The crude products were then purified by silica gel column chromatography (petroleum ether/DCM =3/1 as eluent) to obtain compound **10** (20.0 mg, 16.0%) as a white solid. MS (MALDI-TOF)  $m/z$  calcd for  $\text{C}_{177}\text{H}_{156}$   $[\text{M}]^+$ : 2282.2235, found 2282.2248.

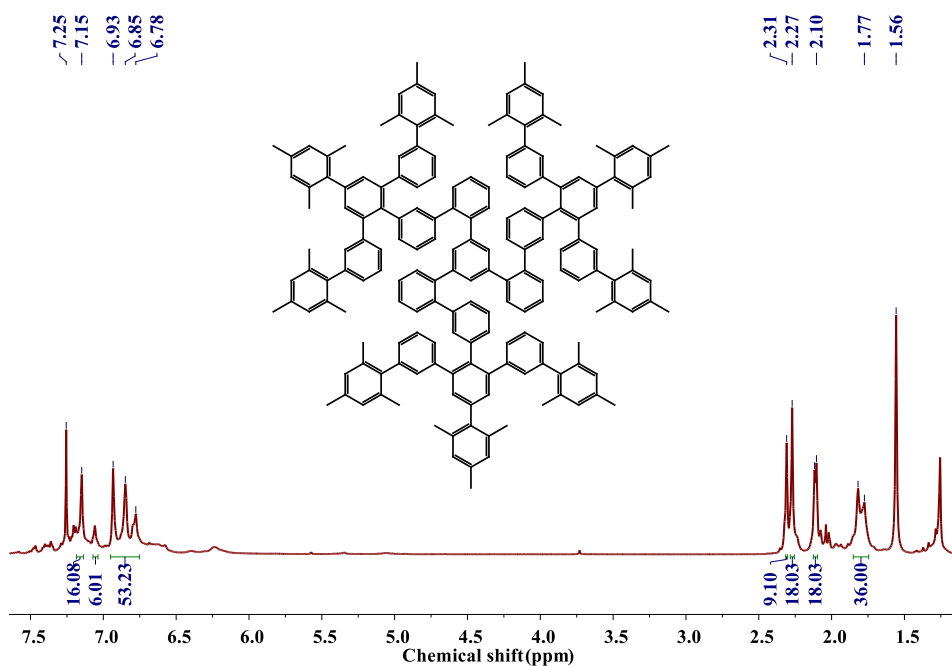


**Figure S10.**  $^1\text{H}$  NMR spectrum of compound **10**. (500 MHz,  $\text{CDCl}_3$ )  $\delta$  7.15 (s, 16H), 7.09 – 7.02 (s, 6H), 6.97 – 6.74 (m, 53H), 2.29 (d,  $J = 18.9$  Hz, 27H), 2.11 (d,  $J = 6.7$  Hz, 18H), 1.80 (d,  $J = 21.8$  Hz, 36H).

**Synthesis of compound MSLG-C96.** To a solution of compound **10** (10.0 mg, 0.00438 mmol) in anhydrous DCM (10 mL) was added  $\text{FeCl}_3$  (160.1 mg, 0.986 mmol) under argon at room temperature. the reaction mixture was stirred for 1 h with continuous  $\text{N}_2$  bubbling. After the mixture was quenched with MeOH, the resulting solution was washed with water and extracted with DCM (10 mL $\times$ 3). The crude product was purified by silica gel column chromatography (petroleum ether/ DCM =2:1 as eluent) to obtain compound **MSLG-C96** (1.50 mg, 15.2%) as a red solid.

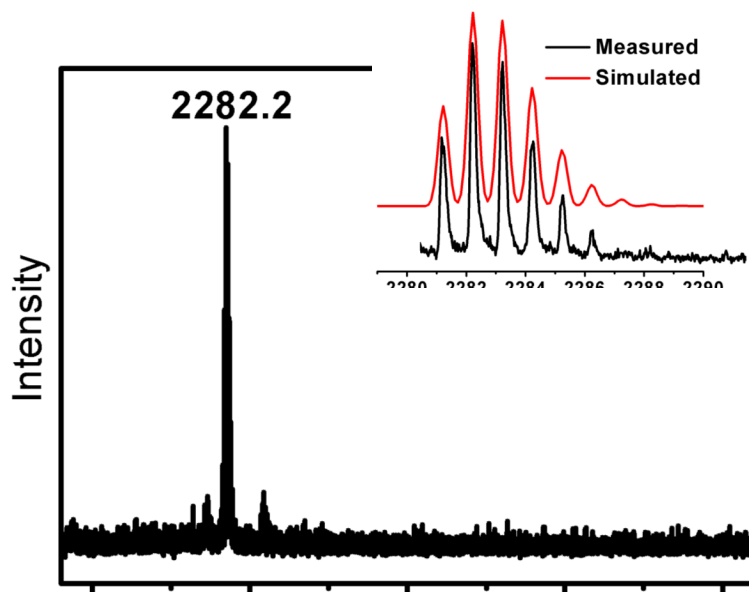


**Figure S11.** MALDI-TOF MS spectrum and simulated data for **compound 10**.

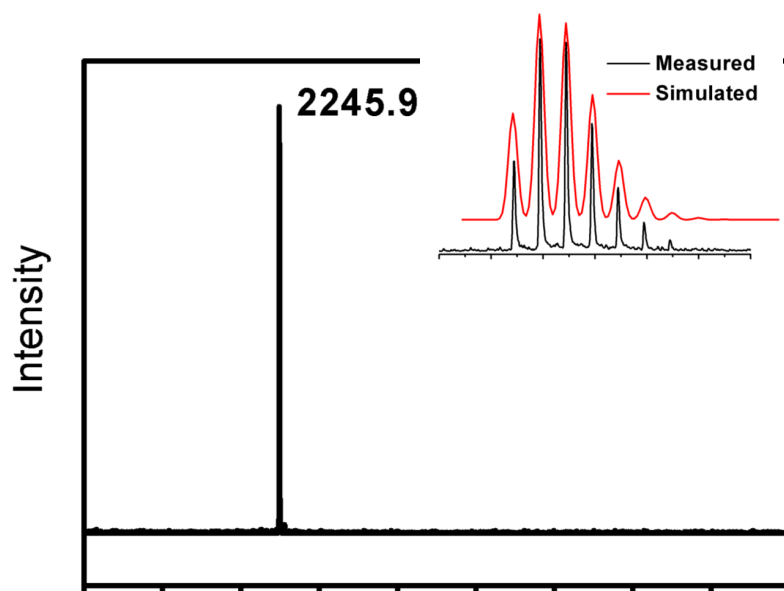


**Figure S12.** MALDI-TOF MS spectrum and simulated data for **MSLG-C96**. Clearly, only the signal of monomer ( $C_{171}H_{121}$ ) was observed without that of stacked oligomers, suggesting the single layer structure of **MSLG-C96**.

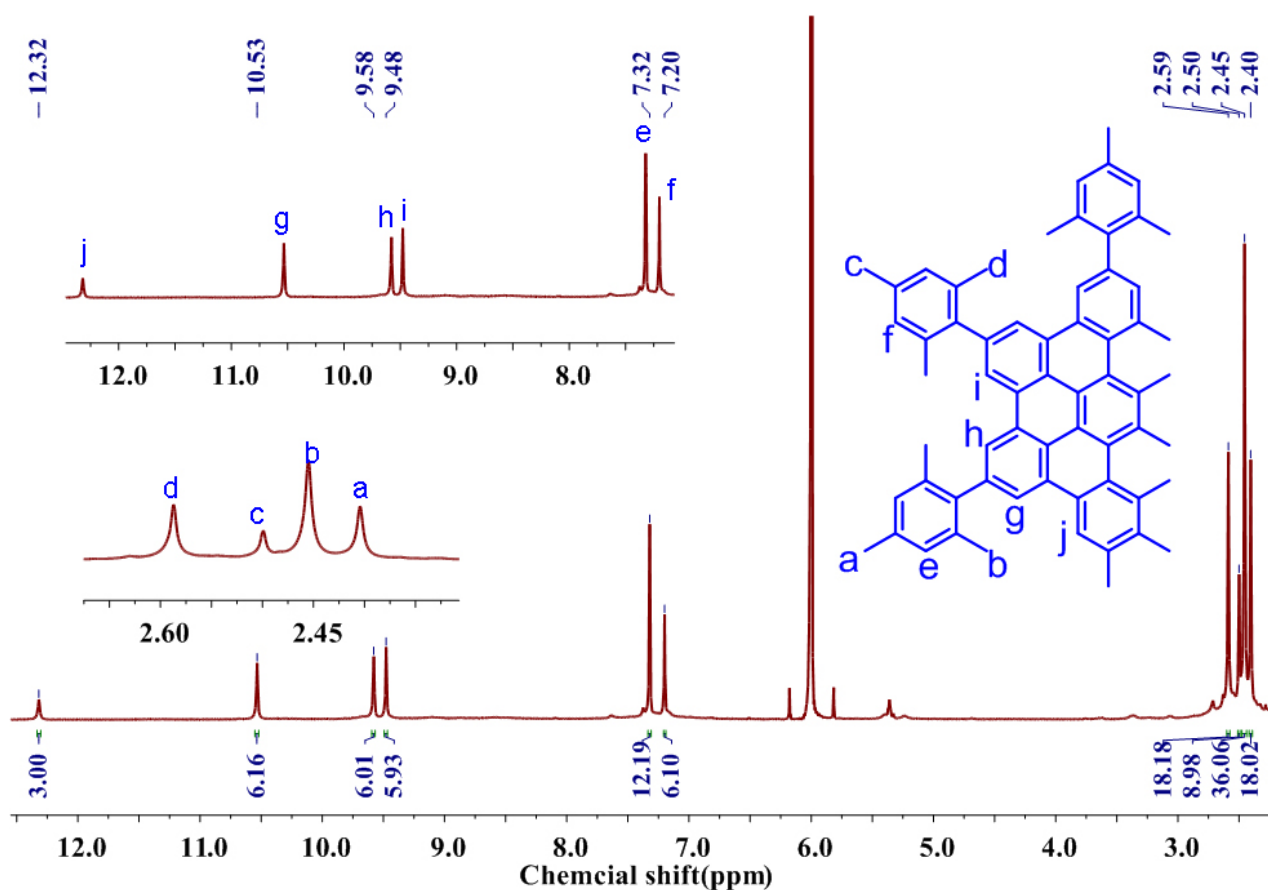


**Figure S13.**  $^1\text{H}$  NMR spectrum of MSLG-C96. According to the chemical shifts, the signals are grouped into four categories. (600 MHz,  $\text{C}_2\text{D}_2\text{Cl}_4$ )  $\delta$  12.32 (s, 3H), 10.53 (s, 6H), 9.58 (s, 6H), 9.48 (s, 6H), 7.32 (s, 12H), 7.20 (s, 6H), 2.59 (s, 18H), 2.50 (s, 9H), 2.45 (s, 36H), 2.40 (s, 6H).ppm. The number and intensity ratio of peaks for the protons of MSLG-C96 reveal a  $D_{3h}$  molecular symmetry, which clearly validates its single layer structure in  $\text{C}_2\text{D}_2\text{Cl}_4$ . All the proton signals were assigned exclusively.

## Section S2 Charge transport through single-molecule junctions

### 2.1 The cross-plane break junction (XPBJ) setup

Nanogaps are prerequisite to fabricate single-molecule junctions, and the scanning tunneling microscopy break junction (STM-BJ) technique is one of the methods to form nanogaps, which is usually employed to construct Au-molecule-Au single-molecule junctions. Herein, we modified our home-built STM-BJ setup to form sandwiched graphene-based single-molecule junctions. In brief, the Au tip and Au substrate were replaced by **O-ring shaped copper wire and copper foil** coating with high-quality chemical vapor deposition (CVD)-grown single-layer graphene.

The schematic diagram of XPBJ setup was shown in Figure S14a. This break junction system contains data collection, signal control, data interaction, and other components, which mainly include a router, data server, FPGA control (Compact RIO 9074, National Instruments, USA), logarithmic amplifier (developed by our group), linear stepper motor (LA-30B-10-F-SP, Harmonic Drive Systems, Japan), motor driver, skeleton, and faraday box. The experimental control system and data acquisition system are achieved by the customized program based on Labview software. PC communicates with the compact RIO through the router. Compact RIO is a programmable automation controller with three modules, AI(analog input), AO(analog output), and DIO(digital input and output). AI module is used to sample the electrical data from the tip passing through the logarithmic amplifier. AO module is responsible for providing bias voltage for the piezo stack and testing. DIO module conducts the displacement of the stepper motor through the motor driver. The logarithmic amplifier and skeleton are placed in a Faraday box to reduce electromagnetic interference of the surrounding environment to the test environment. The skeleton made of hollow cylindrical stainless steel is employed to fix the stepper motor, which can adjust the distance between the tip and the substrate quickly. The piezo stack fixed under the linear stepper motor is used to adjust finely the distance between the tip and the substrate with the bias voltage ranging from 0 to 10 V, resulting in different nanogaps to trap the single molecules. The speed of the tip is about 5 nm/s during approaching and removing the substrate. The conductance of single-molecule junctions was performed at 0.1 V bias voltage via soft contact, in which the conductance feedback ranged from the lower limit of  $10^{-6.5} G_0$  to the upper limit  $10^{-2.5} G_0$ .



stainless steel skeleton through two magnets, 20~30  $\mu\text{L}$  solvent/solution (0.03 mM) was added to the liquid cell. The tip should be aligned with the centre of the hole of the liquid cell. The crash pad in Figure S14b can effectively reduce external mechanical vibration and provide a good conductance measurement environment. The gold substrate shown in Figure S14c was used to connect copper foil into an electrical circuit. After the circuit was closed (Figure S14a), the linear stepper motor and piezo stack are controlled through the threshold set by the self-written program. During the break junction processes, the current was recorded in real-time with a sampling rate of 20 kHz.

## 2.2 Conductance measurement

### 2.2.1 Pure solvent measurement

The conductance measurement of single-molecule junctions was performed in solution at room temperature containing the target molecules with the concentration of 0.03 mM using the XPBJ technique. Here, two mixed pure solvents were used to measure conductance and dissolve the target molecules, one was a mixture of tetrahydrofuran (THF) and decane, and the other was a mixture of 1,1,2,2-tetrachloroethane ( $\text{C}_2\text{H}_2\text{Cl}_4$ ) and carbon tetrachloride ( $\text{CCl}_4$ ). Both THF and  $\text{C}_2\text{H}_2\text{Cl}_4$  are polar solvents, which increase the leakage current. However, polar solvents have to be used to improve the solubility of the target molecules. Therefore, the nonpolar solvents of decane and  $\text{CCl}_4$  were mixed with THF and  $\text{C}_2\text{H}_2\text{Cl}_4$ , respectively, to reduce the leakage current. The volume ratios of THF/decane and  $\text{C}_2\text{H}_2\text{Cl}_4/\text{CCl}_4$  are 1/4 and 1/9, respectively. Besides,  $\text{C}_2\text{H}_2\text{Cl}_4/\text{CCl}_4$  can prevent the aggregation of **MSLG-C96** effectively.

To determine the molecular length, we calculated the stretching distance in mixed solvents of THF/decane and  $\text{C}_2\text{H}_2\text{Cl}_4/\text{CCl}_4$  without target molecules, respectively (Fig. S15). We employed the copper wire coated with graphene as the tip to approach the copper substrate coated with graphene vertically. Since the piezo stack stretched linearly was driven by the applied piezo voltage, the relative displacement of this graphene electrode driven by the piezo stack will be calculated through the recorded piezo voltage changes, and the conversion of piezo voltage to the distance is according to the gold-gold break junction experiment in the same setup<sup>4</sup>. As the data acquisition system recorded the conductance value at each corresponding piezo voltage, therefore, the relative piezo voltage changes can be calculated and summarized when driving the electrode from the conductance value of

$10^{-3.2} G_0$  to  $10^{-5.2} G_0$  repeatedly. One-dimensional (1D) conductance histograms of both THF/decane and  $C_2H_2Cl_4/CCl_4$  from over 1000 individual cycles were obtained in Fig. S15a,d. Fig. S15b,e showed the corresponding histograms of piezo voltage changes with fitted peak center of  $9.98 \times 10^{-4}$  V and  $9.80 \times 10^{-4}$  V for THF/decane and  $C_2H_2Cl_4/CCl_4$ , respectively. Thus, as the piezo voltage enables a 9.8  $\mu$ m distance range within 150 V, the relative displacement of the graphene electrode in the mixed solvents of THF/decane and  $C_2H_2Cl_4/CCl_4$  during the linear conductance range of  $10^{-3.2} G_0$  to  $10^{-5.2} G_0$  will be about 0.27 nm (inset of Fig. S15c,f). Fig. S15c,f gives the two-dimensional (2D) conductance-displacement histogram and piezo distance statistics for THF/decane and  $C_2H_2Cl_4/CCl_4$ . Therefore, when adding molecular solution instead of the solvent, the relative displacement distribution calibrated in the same stretching rate will be in accord with the length of the molecular junction.

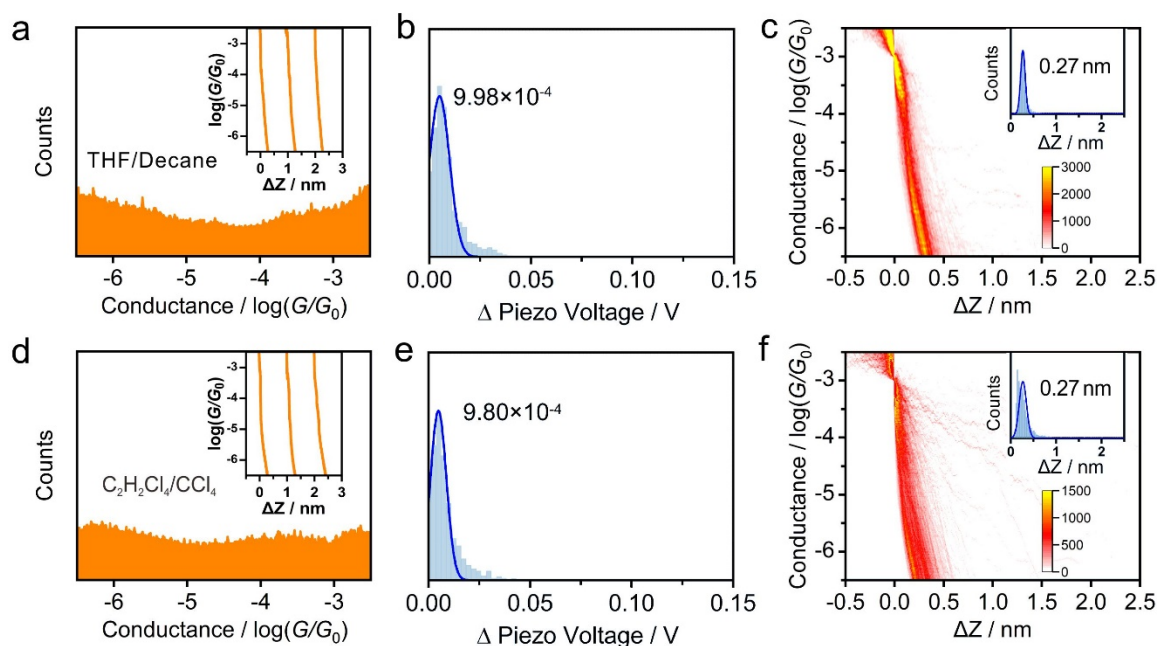


**Figure S15. The electrical properties of mixed pure solvents of THF/decane and  $C_2H_2Cl_4/CCl_4$ .** (a, c) The 1D conductance histograms of mixture solvents of THF/decane (a) and  $C_2H_2Cl_4/CCl_4$  (c). The corresponding insets on the upright were their typical individual traces. (b, e) The histograms of piezo voltage changes with fitted peak centre for THF/decane (b) and  $C_2H_2Cl_4/CCl_4$  (e). (c, f) The 2D conductance-distance histograms of mixed solvents of THF/decane (b) and  $C_2H_2Cl_4/CCl_4$  (d). The corresponding insets on the upright were their plateau distributions with Gaussian fitting.

### 2.2.2 Single-molecule conductance measurement experiments

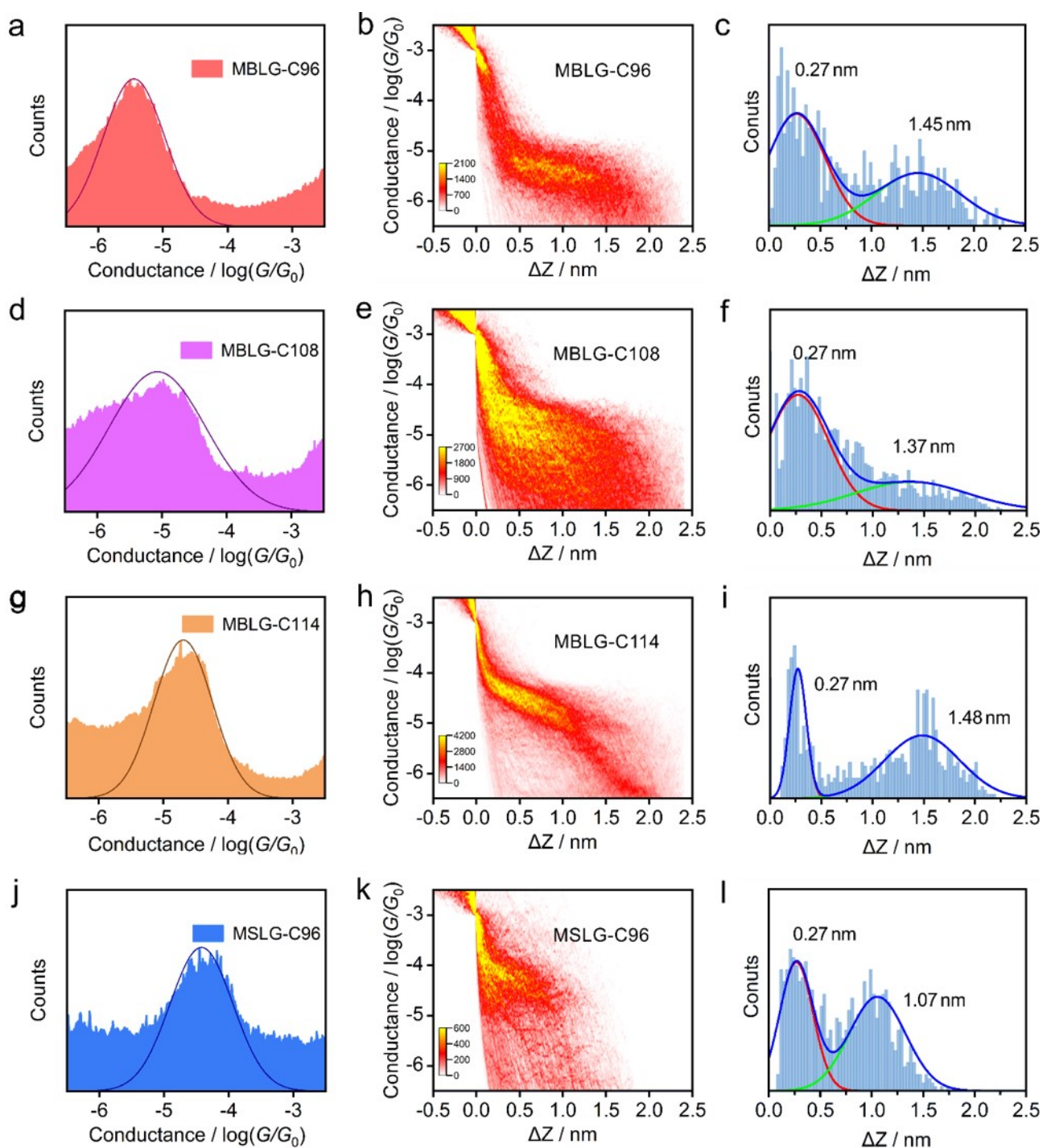


**Figure S16.** The electrical properties of four molecular graphene with directing tunneling and molecular junctions. The 1D conductance histograms of molecular junctions for **MBLG-C96** (a), **MBLG-C108** (d), **MBLG-C114** (g), and **MSLG-C96** (j). The 2D conductance-distance histograms of molecular junctions for **MBLG-C96** (b), **MBLG-C108** (e), **MBLG-C114** (h), and **MSLG-C96** (k). The plateau distributions of molecular junctions for **MBLG-C96** (c), **MBLG-C108** (f), **MBLG-C114** (i), and **MSLG-C96** (l) with Gaussian fitting.

To determine the plateau length of molecular junctions for four molecular graphenes, the charge

transport of molecular junctions containing direct tunneling was investigated in Figure S16. **MBLG-C96**, **MBLG-C108**, and **MBLG-C114** were dissolved in the mixture of THF/decane, while **MSLG-C96** was dissolved in the mixture of C<sub>2</sub>H<sub>2</sub>Cl<sub>4</sub>/CCl<sub>4</sub>. The 1D histograms of four molecular graphenes all showed distinct peaks, indicating the formation of molecular junctions. All the 2D conductance-distance histograms in Figure S16 included direct tunneling and molecular junctions, and the corresponding plateau length distributions were obtained statistically, which conductance range is between  $10^{-5.2} G_0$  to  $10^{-3.2} G_0$ . It is known above that the plateau lengths of the mixed pure solvents were  $\sim 0.27$  nm, which was as a reference to determine the plateau length of molecular junctions for four molecular graphenes. At last, the most probable plateau lengths were obtained by Gaussian fitting.

We calculated the junction formation probability of the four nanographene molecules from over 10,000 conductance traces without data selection. The corresponding 1D, 2D conductance histograms and plateau analysis with Gaussian fitting are shown in Figure S17. The formula is:

$$\text{Probability}(\%) = \frac{\text{Aera}(\text{Molecular junctions, M})}{\text{Aera}(\text{Tunneling junctions, T}) + \text{Aera}(\text{M})}$$

which the Aera(Molecular junctions, M) indicated the area of molecular junctions by the Gaussian fitting, and the Aera(Tunneling junctions, M) indicated the area of Tunneling junctions by the Gaussian fitting. The junction formation probabilities of molecular junctions fabricated by **MBLG-C96**, **MBLG-C108**, **MBLG-C114**, and **MSLG-C96** are 10.53%, 7.96%, 14.89% and 12.68%, respectively.

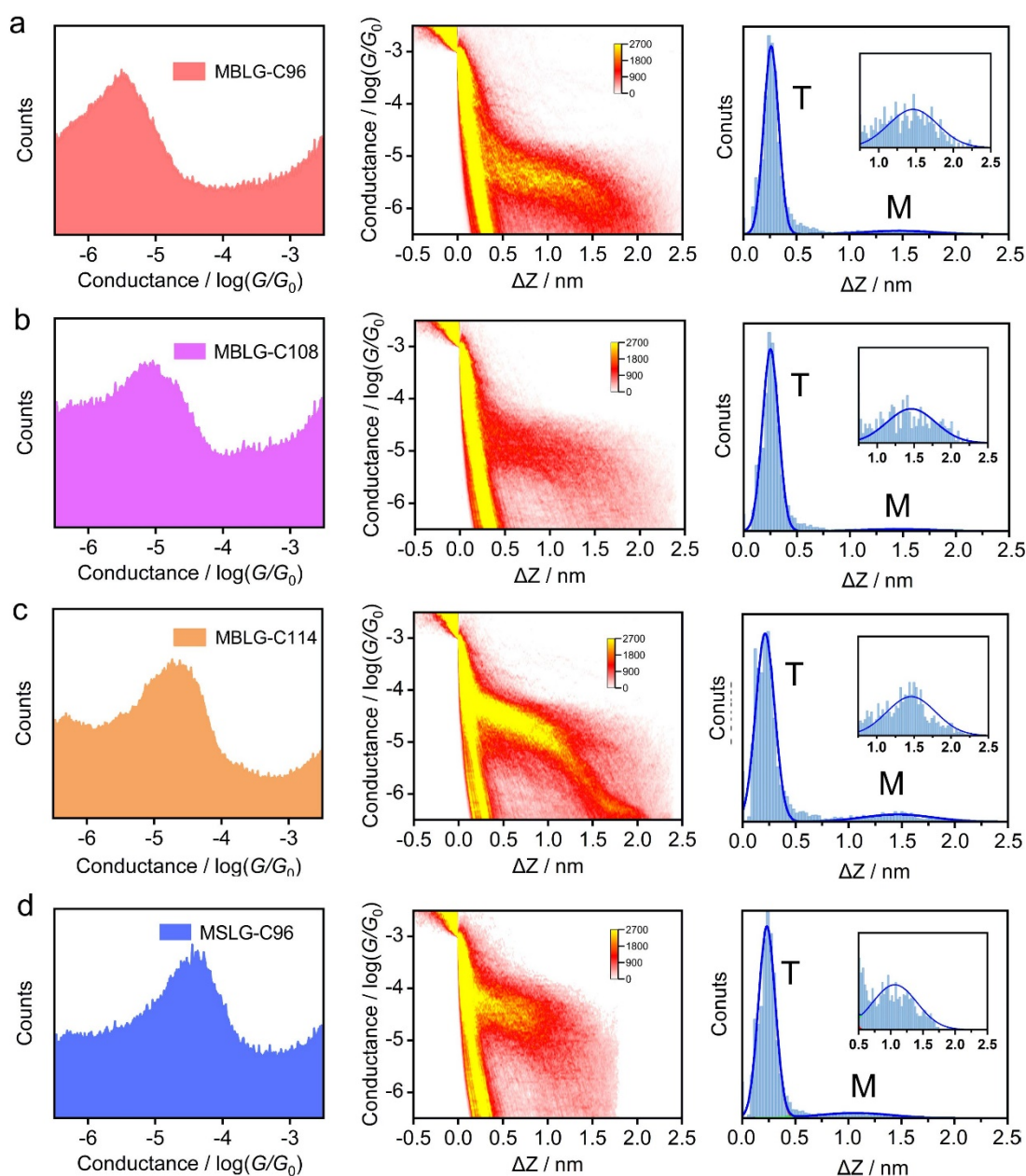


**Figure S17. The 1D, 2D and plateau length analysis for molecular junction without data selection. (a) MBLG-C96. (b) MBLG-C96. (c) MBLG-C96. (d) MBLG-C96.**

Charge transport of molecular junctions based on four molecular graphenes, **MBLG-C96**, **MBLG-C108**, **MBLG-C114**, and **MSLG-C96**, was further investigated. Over  $\sim 1000$  individual conductance traces were selected from 10,000 traces for four molecular graphenes according to the plateau length, and the data was analyzed without any selection. To the 1D conductance histograms in Fig. 2a and Fig. 3b, each molecular junction for four molecular graphenes presented remarkable peaks, and their separated 1D conductance histograms were shown in Figure S18. Gaussian fitting was employed to obtain the most probable conductance value, and the corresponding parameters were listed in Table

S1. In addition, the most probable plateau length value of four molecular-graphene junctions were determined by Gaussian fitting, and the generated parameters of plateau length analysis were list in Table S2. The conductance range selected for the plateau length analysis ranges for **MBLG-C96** is between  $10^{-6.0} G_0$  to  $10^{-4.5} G_0$ , **MBLG-C108** is between  $10^{-5.5} G_0$  to  $10^{-4.0} G_0$ , **MBLG-C114** is between  $10^{-5.2} G_0$  to  $10^{-4.0} G_0$ , and **MSLG-C96** is between  $10^{-5.0} G_0$  to  $10^{-3.8} G_0$ .

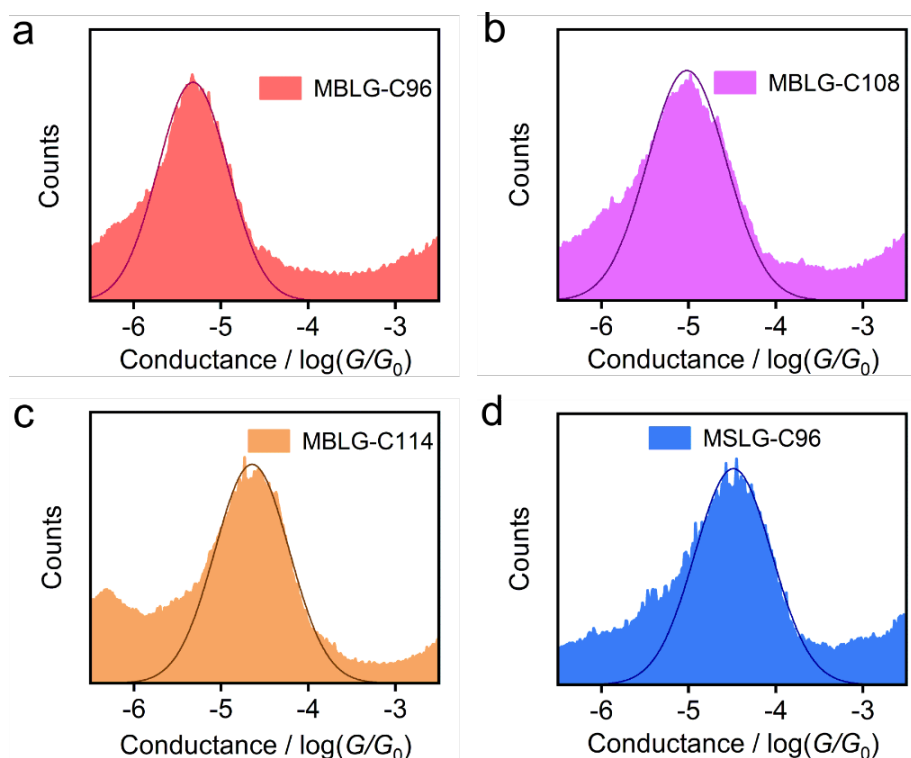


**Figure S18.** The 1D conductance histograms of the molecular junctions for four molecular graphene.

Over 1000 individual traces showing the molecular plateau are selected from  $\sim 10,000$  curves according to the plateau length of molecular junctions. Figure S19 showed the average change of junction formation probability per half hour during five-hour testing. The highest junction formation probability is 29.47% from 3.5 h to 4.0 h for MBLG-C114, and the junction formation probability of four nanographene molecules usually decays after 3 h or 4 h. The corresponding 1D, 2D conductance histograms, and plateau length analysis of each 0.5 h in Figure S19 are shown in Figures S20-S23.

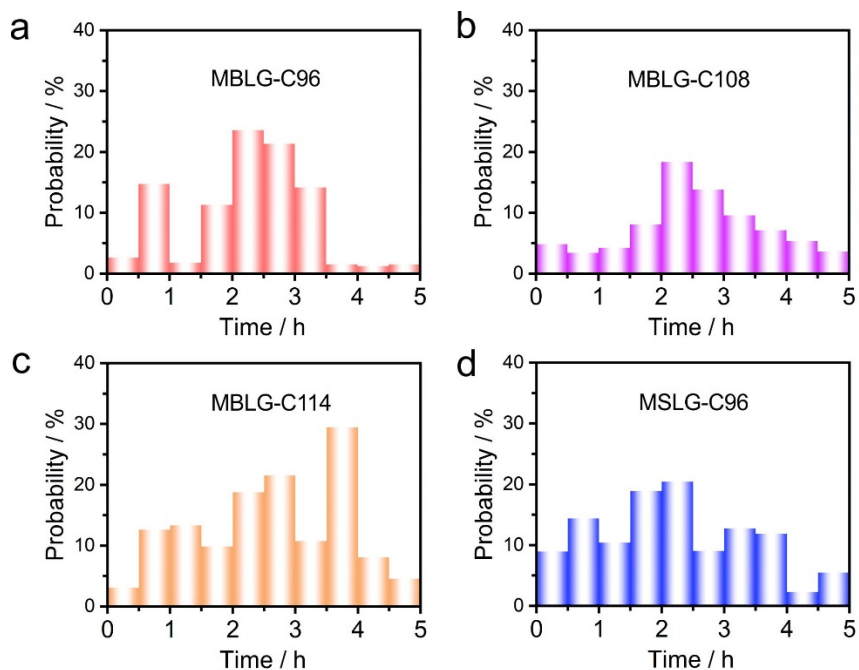


**Figure S19. Junction formation probability of four nanographene molecules versus time. a. MBLG-C96. b. MBLG-C108. c. MBLG-C114. d. MSLG-C96.**

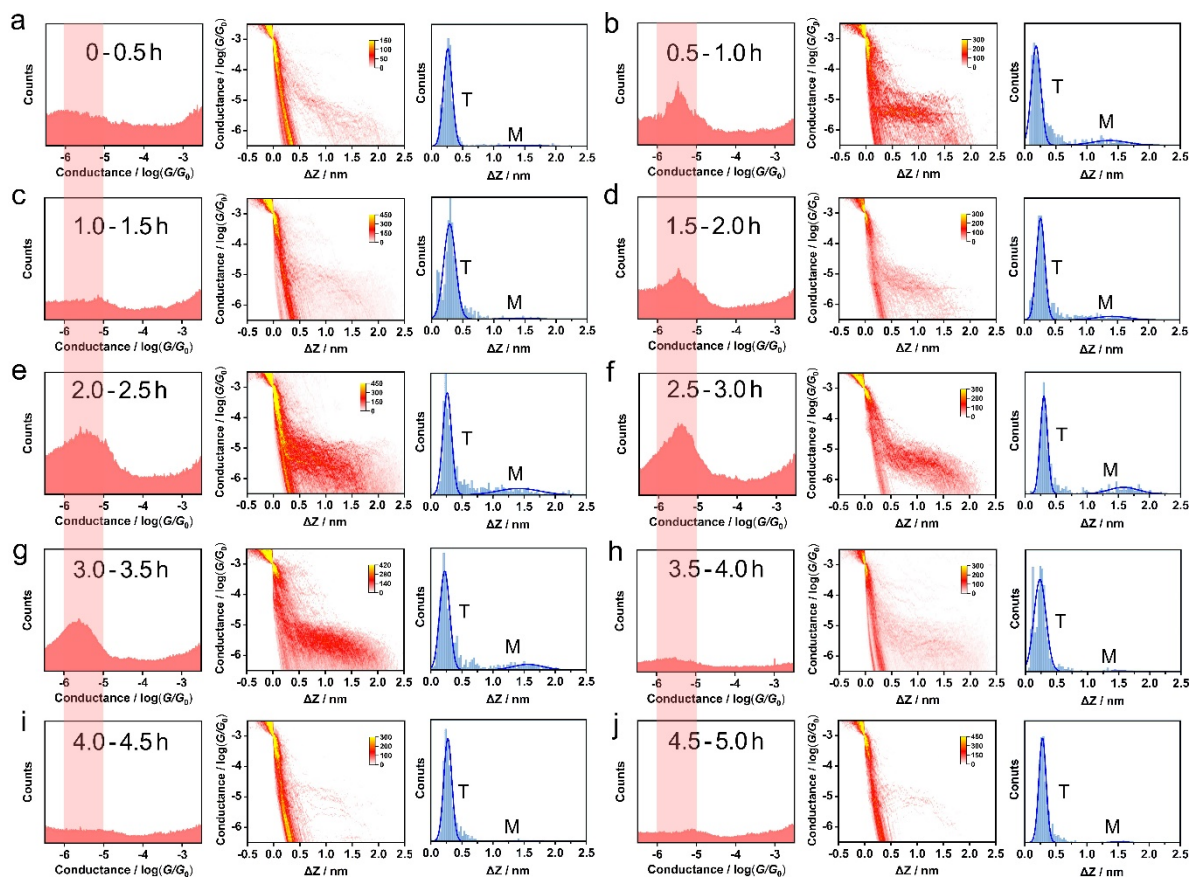


**Figure S20. The 1D, 2D histograms, and plateau analysis of MBLG-C96 at different times.**

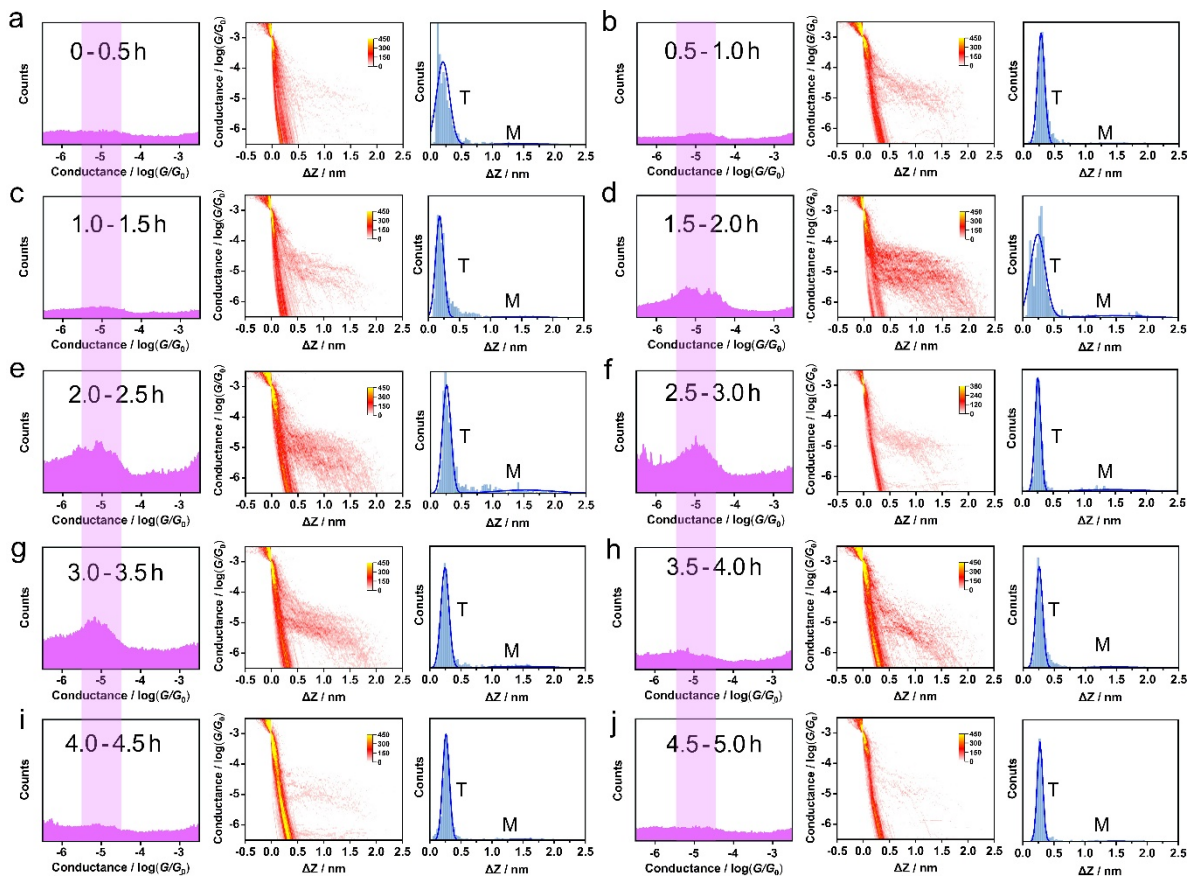


**Figure S21. The 1D, 2D histograms, and plateau analysis of MBLG-C108 at different times.**

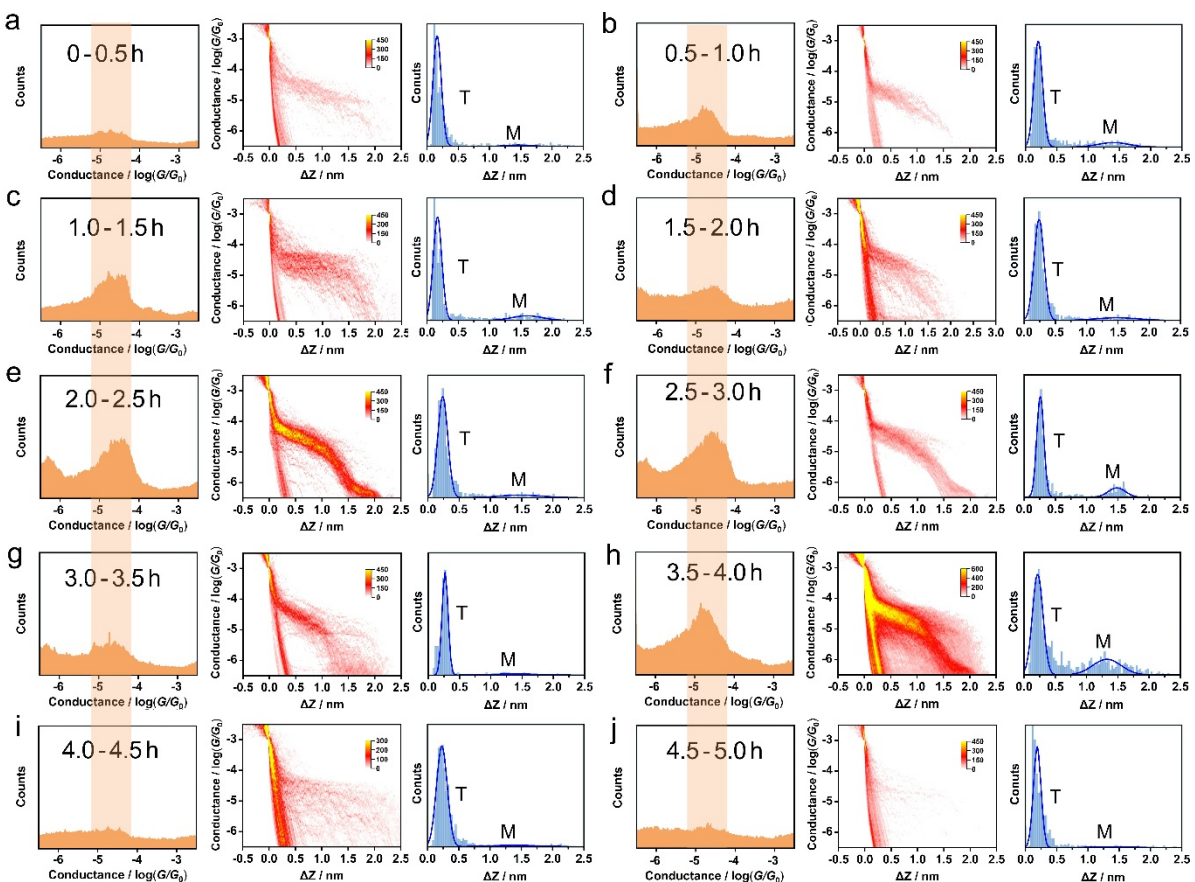


**Figure S22. The 1D, 2D histograms, and plateau analysis of MBLG-C114 at different times.**

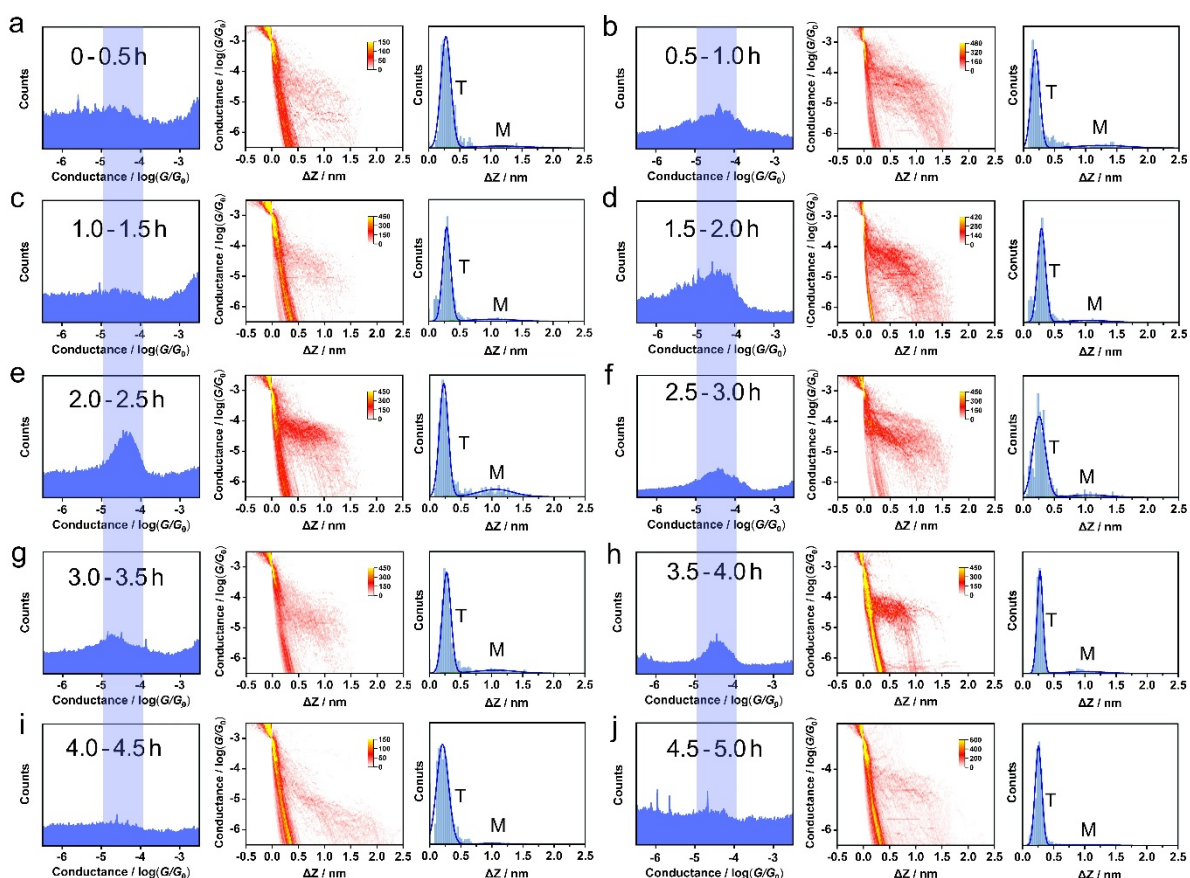


**Figure S23. The 1D, 2D histograms, and plateau analysis of MSLG-C96 at different times.**

The degree of freedom for modulating intradimeric interactions are twist angle and intradimeric distance. Due to the steric hindrance, the twist angle is fixed by their side groups with negligible impact during the pulling process. Moreover, the degree of freedom for fluctuation of intradimeric distance is limited in angstrom scale. Otherwise, we would observe the dissociation of dimer and formation of monolayer during break junction. From the data, we could not find any feature of the formation of the monolayer, both in conductance and relative distance histograms. In contrast with that, the formation of the bilayer was found in the data of the monolayer, as shown in Fig. 3. It proves that the bilayer structure is more stable during break junction. Therefore, the intradimeric interaction could not account for the conductance fluctuation during the pulling process.

Based on our theoretical results, we think the interfacial change dominates the variation of conductance during the pulling process. As the plot of total energy versus interfacial distance shown in Figure S27, the slope of MBLG-C108 after the local minimum point is the smallest among the three compounds. It means that the interfacial distance of MBLG-C108 is more sensitive to the pulling during break junction.

Another hypothesis accounting for this phenomenon is that transport through MBLG-C108 is contributed by two different pathways, including a direct tunneling pathway and a molecular-mediated pathway because of its hollow structure. The contribution of the tunneling pathway is more sensitive to the pulling process, and it dominates the early stage of pulling.

A quantitative description of the conductance plateau is vital for gaining a deep understanding of evolution during the pulling process. To clarify this point, we added the fitted averaged conductance-distance traces and the distribution of conductance variations (i.e. standard deviation) in the plateau range of 0.5 to 1.0 nm during stretching for four nanographene molecules in Figure S24. The standard deviation of MBLG-C108 is the largest among the three bilayer graphene molecules, indicating that MBLG-C108 is the most sensitive to the pulling process. The standard deviation of MSLG-C96 is greater than the other bilayer graphene molecules, indicating that the interfacial change dominates the variation of conductance during the pulling process.

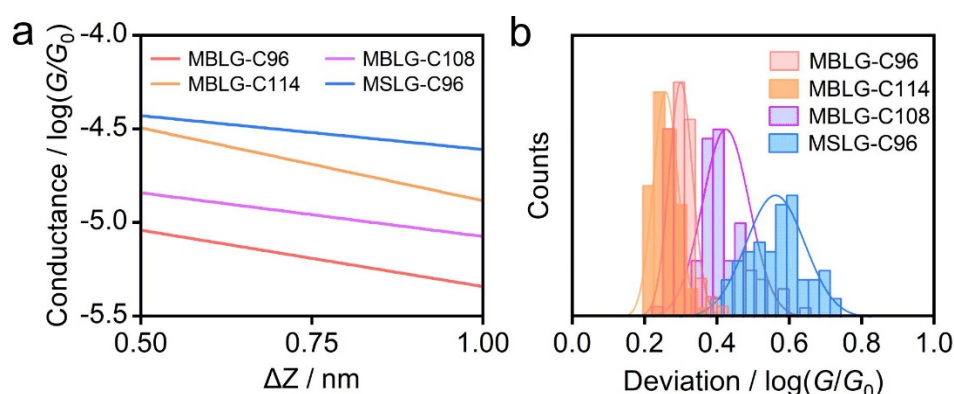


**Figure S24.** (a) The fitted averaged conductance-distance traces. (b) Distribution of conductance variations in the plateau range of 0.5 to 1.0 nm during stretching.

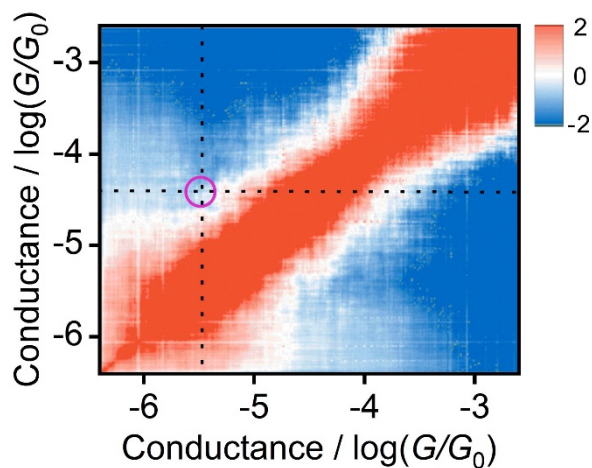
**Table S1. Generated parameters of the 1D histogram of molecular junctions for four molecular graphene.**

<b>Molecule</b>	<b>Centre / <math>\log(G/G_0)</math></b>	<b>Sigma</b>	<b>FWHM</b>
<b>MBLG-C96</b>	-5.32	0.377	0.888
<b>MBLG-C108</b>	-5.02	0.452	1.064
<b>MBLG-C114</b>	-4.65	0.427	1.006
<b>MSLG-C96</b>	-4.49	0.442	1.041

**Table S2. Generated parameters of plateau length analysis of molecular junctions for four molecular graphene.**

<b>Molecule</b>	<b>Centre / nm</b>	<b>Sigma</b>	<b>FWHM</b>
<b>MBLG-C96</b>	1.47	0.260	0.613
<b>MBLG-C108</b>	1.37	0.379	0.892
<b>MBLG-C114</b>	1.48	0.162	0.380
<b>MSLG-C96</b>	1.07	0.190	0.448

To explore the correlation of HC and LC for MSLG-C96 in THF/decane, 2D cross-correlation histogram is constructed as shown in Figure S25. The two conductances of HC and LC states are  $10^{4.48} G_0$  and  $10^{-5.41} G_0$  resulting from 1D conductance histogram, and an uncorrelated region locating at  $[10^{-4.48} G_0, 10^{-5.41} G_0]$  is found, which indicated the appearance of each conductance state is independent during the XPBJ process.

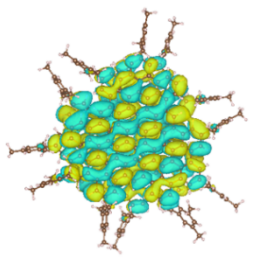
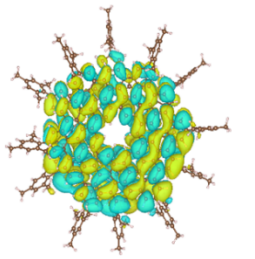
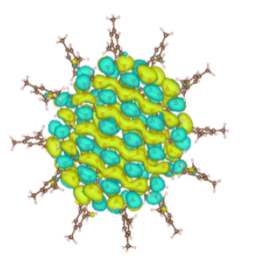
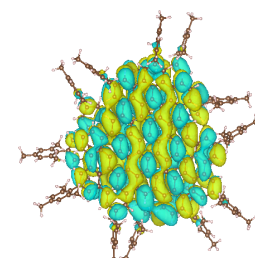
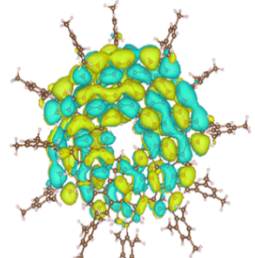
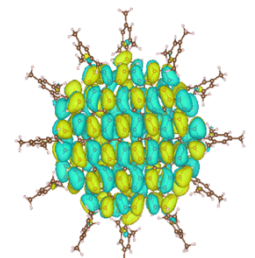
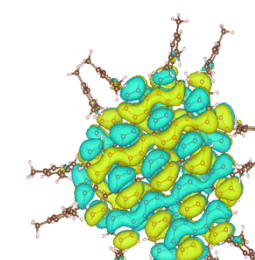
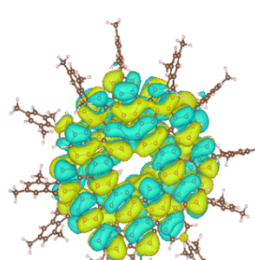
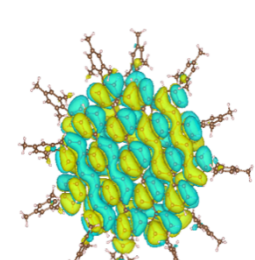
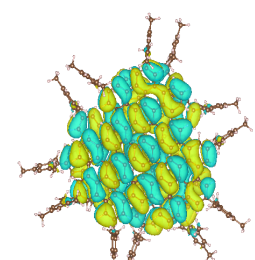
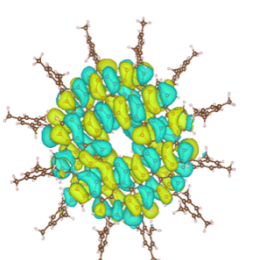
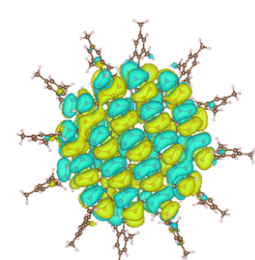


**Figure S25. 2D cross-correlation histogram analysis of HC and LC for MSLG-C96.**

## Section S3 Theoretical calculation

The DFT calculations for Molecular Bilayer Layer Graphene (MBLG) flakes.

Table S3. The wave functions and the HUMO-LUMO gap for MBLG-C96, MBLG-C108, and MBLG-C114.

	MBLG-C96	MBLG-C108	MBLG-C114
LUMO+1			
E (eV)	-2.71	-2.65	-2.80
LUMO			
E / eV	-2.71	-2.65	-2.81
<b>HOMO-LUMO gap (eV)</b>	<b>1.62</b>	<b>1.88</b>	<b>1.45</b>
HOMO			
E / eV	-4.33	-4.53	-4.26
HOMO-1			
E / eV	-4.33	-4.53	-4.26

### Configurations between the two graphene sheets and the MBLGs.

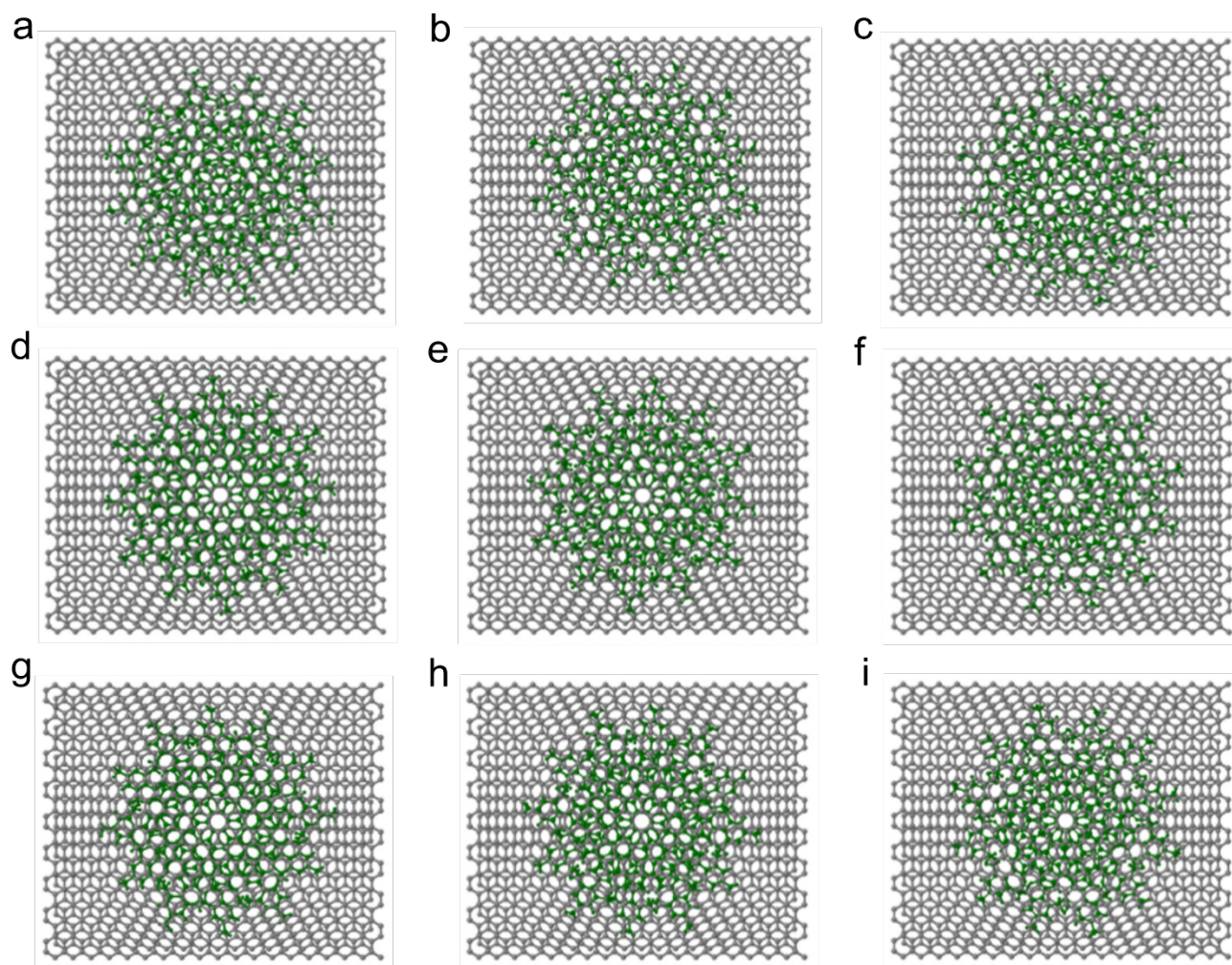


**Figure S26.** Different configurations between MBLGs and the graphene sheets from top view.

(a) Top-Hollow position. The C atom of the graphene sheet overlaps with the center of **MBLG-C114** from top view. (b) Hollow-Hollow position. The center of **MBLG-C114** was shifted from the position in (a) to up by 1.42 Å. (c) The center of **MBLG-C114** was shifted from the position in (a) to the right by 1.23 Å. (d) The geometry obtained by rotating the molecule by 10° based on junction (b). (e) The geometry obtained by rotating the molecule by 20° based on junction (b). (f) The geometry obtained by rotating the molecule by 30° based on junction (b). (g) The geometry obtained by rotating the molecule by 40° based on junction (b). (h) The geometry obtained by rotating the molecule by 50° based on junction (b). (i) The geometry obtained by rotating the molecule by 60° based on junction (b). Nine configurations are considered in our calculations between the MBLGs and the graphene sheets. The green color is used to distinguish the molecule (in this case **MBLG-C114**) from the graphene sheets (grey color).

The transmission spectra for MBLGs before the side groups are rotated.

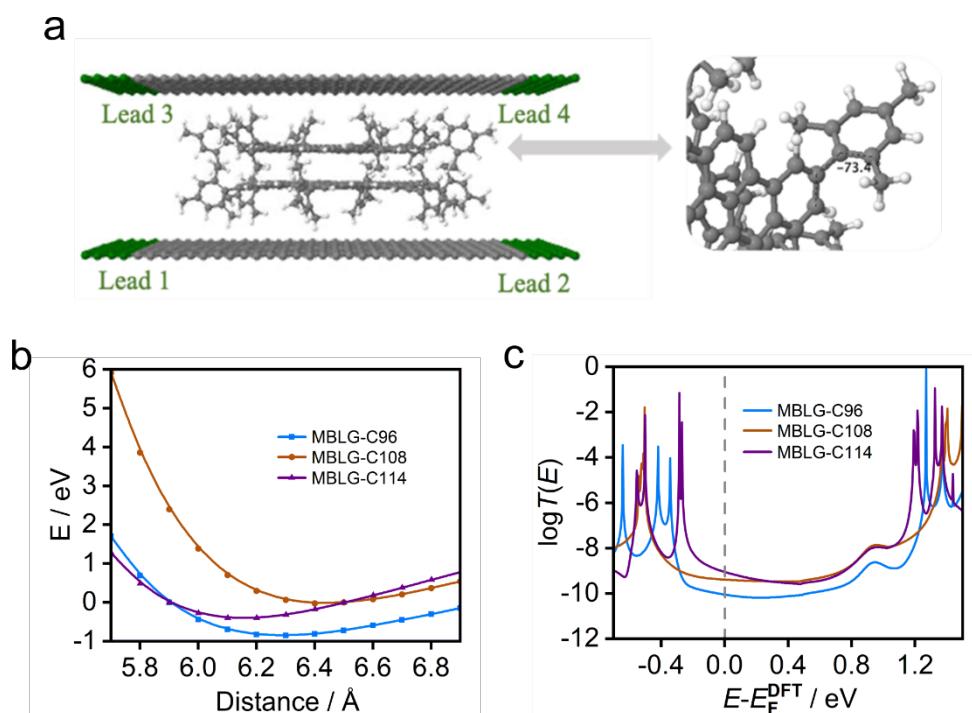


**Figure S27.** Transport properties of MBLG molecules. (a) Sandwiched structure of the molecular junction of MBLG-C114. (b) Evolutions of total energy versus distance between graphene flake of MBLG and one graphene sheet for MBLG-C96, MBLG-C108, and MBLG-C114. The minimum total energies for MBLG-C96, MBLG-C108, and MBLG-C114 are at 6.3  $\text{\AA}$ , 6.4  $\text{\AA}$  and 6.2  $\text{\AA}$ , respectively between the lower flake of MBLG molecule and the bottom graphene. (c) Transmission spectra of MBLG-C96, MBLG-C108, and MBLG-C114.

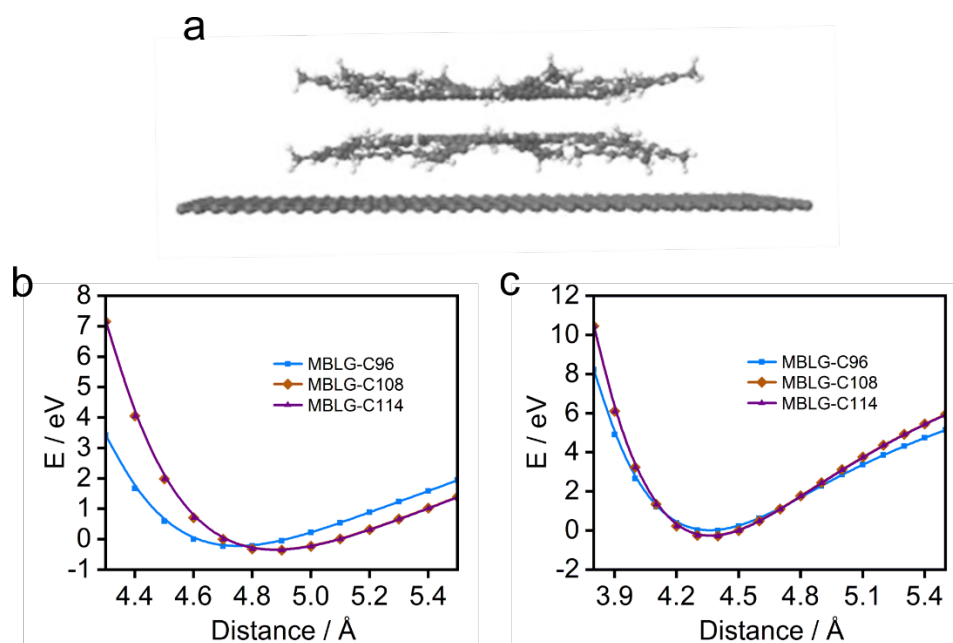


**Figure S28.** Total energy  $E$  (after subtracting a large negative number for simplicity) versus the distances between the bottom graphene sheet and lower graphene flake of MBLGs with the side groups rotated to  $30^\circ$  and  $10^\circ$  relative to the graphene flake. (a) Structure of MBLG-C96 lying on the graphene sheet. (b) Evolutions of total energy versus distance between graphene flake of MBLG and one graphene sheet for MBLG-C96, MBLG-C108, and MBLG-C114 where the side groups rotated to  $30^\circ$ . (c) Evolutions of total energy versus distance with the side groups rotated to  $10^\circ$ .

## The transmission spectra after rotating the side groups to 10° and 30°

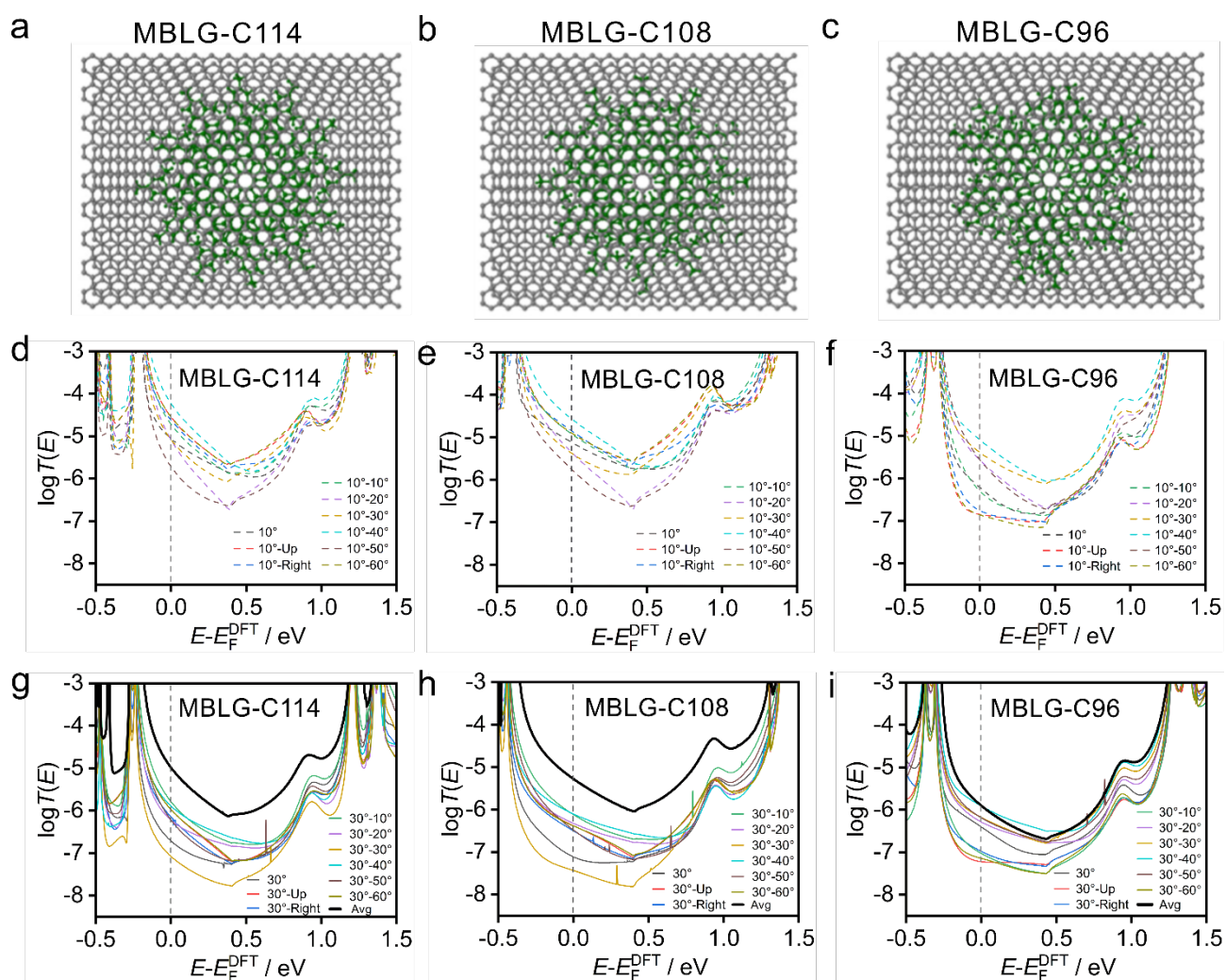
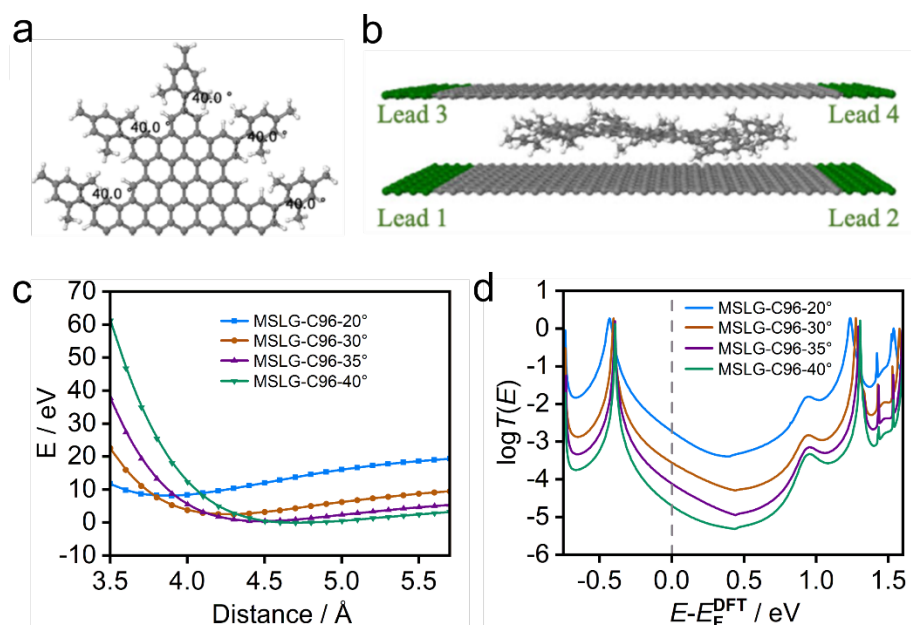


**Figure S29.** DFT-based transmission functions of several configurations of MBLGs with side groups rotated to 10° and 30° relative to the graphene flake. (a-c) Top view of the molecular junction of MBLG-C114 (a), MBLG-C108 (b) and MBLG-C96 (c). (d-f) Transmission spectra of the different geometries of MBLG-C114 (d), MBLG-C108 (e) and MBLG-C96 (f) as rotating the side groups to 10° relative to the graphene flake (dotted curves). (g-i) Transmission spectra of the different geometries of MBLG-C114 (g), MBLG-C108 (h) and MBLG-C96 (i) as rotating the side groups to 30° relative to the graphene flake (solid curves) and average of all 18 transmission curves (black solid curve). The 18 transmission curves are the transmission spectra for different structures shown in Figure S26 with the side groups rotated to 10° and 30°.

## The DFT calculations of MSLG-C96.

### Rotating the side groups of MSLG-C96 to 20°, 30°, 35° and 40° relative to the graphene flake of MSLG-96.

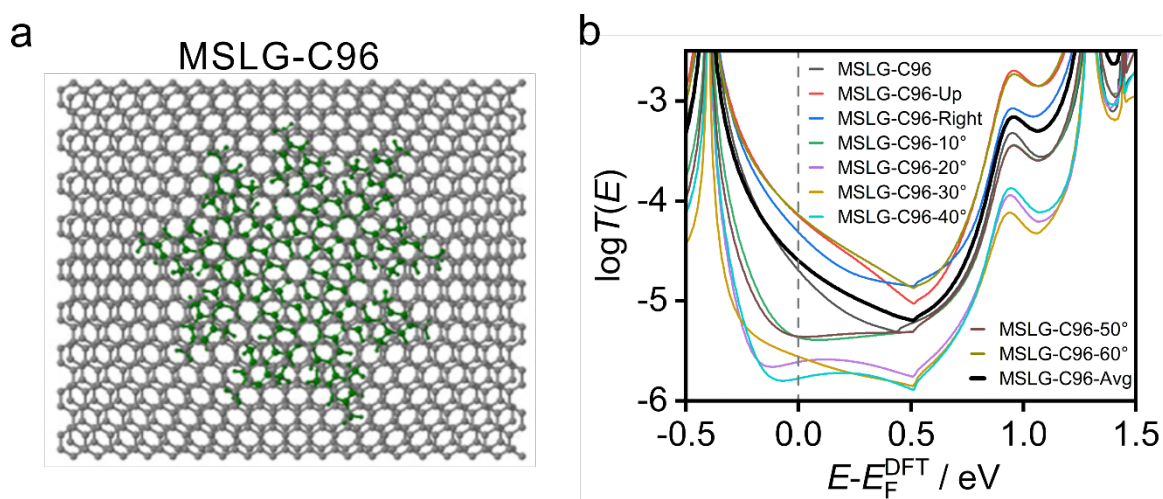
Figure S30a illustrates the angle between the graphene flake and peripheral mesityl groups, which we manually rotated to different angles. Figure S30c presents the evolutions of the total energy against the distance between the bottom graphene sheet and the flake plane of the MSLG-C96 molecule. The side groups of MSLG-C96 are manually rotated to different angles (20°, 30°, 35°, and 40°). At the angles, 20° (blue line), 30° (orange line), 35° (purple line), 40° (green line), the minimum total energy is found at a distance 3.9 Å, 4.3 Å, 4.5 Å, 4.7 Å, respectively. Based on these distances, the molecular junctions of MSLG-C96 are built. The corresponding transmission functions are calculated for MSLG-C96 with different rotation angles, and the results are shown in Figure S26d. The transmission functions increase significantly when the angles decrease from 40° to 20° in the whole HOMO-LUMO gap; the black horizontal dashed line shows the experimental result and Fermi energy  $E_F$  is shown by the black vertical dashed line, which is predicted by DFT.



**Figure S30.** Theoretical simulations for Molecular Single-Layer Graphene of C96. (a) The angle between the graphene flake and peripheral mesityl groups of MSLG-C96. (b) The sandwiched structure of the molecular junction of MSLG-C96. (c) Total energy versus distance between the graphene flake of MSLG-C96 and the bottom graphene sheet, in which the side groups of MSLG are rotated to different angles 20°, 30°, 35°, and 40°, relative to the flake. (d) Transmission spectra of geometries with varying angles of rotation.

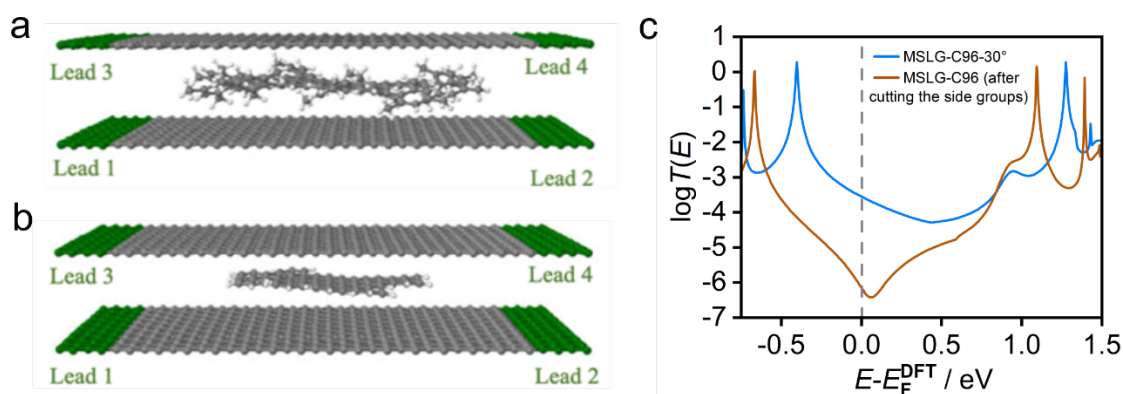
### The transmission spectra of different geometries for MSLG-C96.

Figure S31a Shows the lateral view of the molecular junction of the single-layer (green colour) where the side groups rotated to  $40^\circ$ . After that, we calculate the transmission coefficients for nine different geometries, which mentioned in Section S1, (a) blue curve, (b) orange curve, (c) purple curve, (d) green curve, (e) yellow curve, (f) light blue curve, (g) grey curve), (h) pink curve, (i) light green curve, and the average of all these transmission curves (black curve) which are presented in Figure S31b.



**Figure S31.** Transmission spectra of several configurations of MSLG of C96 with side groups rotated to  $40^\circ$ . (a) Top view of the molecular junction of MSLG-C96. (b) Transmission spectra of different geometries.

## Cutting the side groups for MSLG-C96.



**Figure S32.** Theoretical simulations for MSLG-C96 with side groups that rotated to 30° and without it. (a) The sandwiched structure for MSLG-C96 with side groups rotated to 30°. (b) The sandwiched structure for MSLG-C96 after manually cutting the side groups. (c) DFT-based transmission functions for MSLG-C96 with side groups (blue curve) and MSLG-C96 after cutting the side groups (brown curve).

## References

1. X.-J. Zhao, H. Hou, X.-T. Fan, Y. Wang, Y.-M. Liu, C. Tang, S.-H. Liu, P.-P. Ding, J. Cheng, D.-H. Lin, C. Wang, Y. Yang and Y.-Z. Tan, *Nat. Commun.*, 2019, **10**, 3057.
2. X. J. Zhao, H. Hou, P. P. Ding, Z. Y. Deng, Y. Y. Ju, S. H. Liu, Y. M. Liu, C. Tang, L. B. Feng and Y. Z. Tan, *Sci. Adv.*, 2020, **6**, eaay8541.
3. S. S. Cui, G. L. Zhuang, D. P. Lu, Q. Huang, H. X. Jia, Y. Wang, S. F. Yang and P. W. Du, *Angew. Chem. Int. Ed.*, 2018, **57**, 9330-9335.
4. W. Hong, D. Z. Manrique, P. Moreno-García, M. Gulcur, A. Mishchenko, C. J. Lambert, M. R. Bryce and T. Wandlowski, *J. Am. Chem. Soc.*, 2012, **134**, 2292-2304.